

The dusty heart of nearby active galaxies

I. High-spatial resolution mid-IR spectro-photometry of Seyfert galaxies^{*}

S. F. Hönig^{1,2}, M. Kishimoto¹, P. Gandhi³, A. Smette⁴, D. Asmus^{4,5}, W. Duschl^{5,6}, M. Polletta⁷, and G. Weigelt¹

¹ Max-Planck-Institut für Radioastronomie, Auf dem Hügel 69, 53121 Bonn, Germany

² University of California in Santa Barbara, Department of Physics, Broida Hall, Santa Barbara, CA 93106, USA
e-mail: shoenig@physics.ucsb.edu

³ RIKEN Cosmic Radiation Lab, 2-1 Hirosawa, Wakoshi Saitama 351-0198, Japan

⁴ European Southern Observatory, Casilla 19001, Santiago 19, Chile

⁵ Institut für Theoretische Physik und Astrophysik, Christian-Albrechts-Universität zu Kiel, Leibnizstr. 15, 24098 Kiel, Germany

⁶ Steward Observatory, The University of Arizona, 933 N. Cherry Ave, Tucson, AZ 85721, USA

⁷ INAF - IASF Milano, via E. Bassini, 20133 Milano, Italy

Received 26 November 2009 / Accepted 26 February 2010

ABSTRACT

In a series of papers, we aim at stepping towards characterizing physical properties of the AGN dust torus by combining IR high-spatial resolution observations with 3D clumpy torus models. In this first paper, we present mid-IR imaging and 8–13 μm low-resolution spectroscopy of nine type 1 and ten type 2 AGN. The observations were carried out with the VLT/VISIR mid-IR imager and spectrograph and can be considered the largest currently available mid-infrared spectro-photometric data set of AGN at spatial resolution $\lesssim 100$ pc. These data resolve scales at which the emission from the dust torus dominates the overall flux, and emission from the host galaxy (e.g. star-formation) is resolved out in most cases. The silicate absorption features are moderately deep and emission features, if seen at all, are shallow. The strongest silicate emission feature in our sample shows some notable shift of the central wavelength from the expected 9.7 μm (based on ISM extinction curves) to ~ 10.5 μm . We compare the observed mid-IR luminosities of our objects to AGN luminosity tracers (X-ray, optical and [O III] luminosities) and find that the mid-IR radiation is emitted quite isotropically. In two cases, IC 5063 and MCG–3–34–64, we find evidence for extended dust emission in the narrow-line region. We confirm the correlation between observed silicate feature strength and Hydrogen column density, which was recently found in *Spitzer* data at lower spatial resolution. In a further step, our 3D clumpy torus model has been used to interpret the data. We show that the strength of the silicate feature and the mid-IR spectral index α can be used to get reasonable constraints on the radial dust distribution of the torus and the average number of clouds N_0 along an equatorial line-of-sight in clumpy torus models. The mid-IR spectral index α is almost exclusively determined by the radial dust distribution power-law index a , while the silicate feature depth mostly depends on N_0 and the torus inclination. A comparison of model predictions to our type 1 and type 2 AGN reveals that average parameters of $a = -1.0 \pm 0.5$ and $N_0 = 5 - 8$ are typically seen in the presented sample, which means that the radial dust distribution is rather shallow. As a proof-of-concept of this method, we compared the model parameters derived from α and the silicate feature strength to more detailed studies of full IR SEDs and interferometry and found that the constraints on a and N_0 are consistent. Finally, we may have found evidence that the radial structure of the torus changes from low to high AGN luminosities towards steeper dust distributions, and we discuss implications for the IR size-luminosity relation.

Key words. galaxies: Seyfert – galaxies: nuclei – galaxies: active – infrared: galaxies – X-rays: galaxies

1. Introduction

The dust torus is one of the key ingredients of the unification scheme of AGN (Antonucci 1993; Urry & Padovani 1995). It must be pointed out, though, that in recent years the torus picture has evolved away from a “donut” towards a more general circumnuclear, geometrically- and optically-thick dust distribution. The dust reprocesses the optical/UV photons of the accretion disk and re-emits the received energy in the infrared (IR). Thus, the torus can be directly studied through the IR emission of AGN, unless the AGN is radio-loud. Within the last years, investigations based on IR spectral energy distributions (SEDs) characterized the torus emission and confirmed the basic picture of the unification scheme. Most notable are the silicate features

at 10 and 18 μm which are generally seen in absorption in type 2 AGN and in emission in type 1 objects.

However, more detailed studies – mainly using data from the IRS and MIPS instruments on-board the *Spitzer* satellite – revealed subtle differences to model predictions. In particular, silicate emission features in type 1 AGN are much weaker than expected from early torus models, which used smooth dust distributions. As shown in the literature, this might be explained by clumpiness of the dust in the torus, which leads to an overall suppression of the emission feature (Nenkova et al. 2002; Dullemond & van Bemmelen 2005; Hönig et al. 2006; Schartmann et al. 2008; Nenkova et al. 2008; Hönig & Kishimoto 2010). However, as will be shown in the second paper of this series (Hönig & Kishimoto 2010, pre-print available on astro-ph), weak emission features are not a generic property of clumpy torus models but might be used to constrain some model parameters of the dust distribution in clumpy tori.

^{*} Based on ESO observing programs 078.B-0303, 080.B-0240, 280.B-5068, 082.B-0299, and 083.B-0239.

One of the problems of *Spitzer* is the comparably low spatial resolution of $\sim 3''$ at $10\ \mu\text{m}$. On the other hand, the torus near- and mid-IR emission originates from the inner few parsecs around the AGN, which corresponds to $< 0.1''$ even for the nearest Seyfert galaxies. As a result, the *Spitzer* data are prone to contamination from the host galaxy or circumnuclear star formation, which can be identified by strong PAH emission lines. One way to overcome this problem is a decomposition of the data into several components. But this requires good knowledge about the generic SEDs of each component, which is, of course, difficult when aiming at characterizing the torus emission, and introduces additional parameters, which in turn leads to parameter degeneracies.

The most direct way of studying the dust torus is IR interferometry. Recently, the IR emission source in a small number of nearby type 1 and type 2 AGN have been resolved in the mid-IR with the interferometric instrument MIDI at the VLTI (Jaffe et al. 2004; Tristram et al. 2007; Beckert et al. 2008; Raban et al. 2009; Tristram et al. 2009; Burtcher et al. 2009) and in the near-IR with the Keck interferometer (Swain et al. 2003; Kishimoto et al. 2009a). While interferometry provides the most direct access to the torus structure and brightness distribution (Kishimoto et al. 2009a), observations are limited to the brightest AGN that are in reach of current facilities. A compromise between *Spitzer* and interferometry can be achieved by using ground-based 8 m-class single telescopes. These observations usually do not have the potential of firmly resolving the torus, but may isolate the nuclear dust emission from any contaminating source in the host galaxy (e.g. Horst et al. 2009; Gandhi et al. 2009; Mason et al. 2009). Following this approach, we observed 19 nearby AGN with the mid-infrared imager and spectrograph VISIR at the ESO Very Large Telescope (VLT) Paranal Observatory. In this first paper of our series, we present results from mid-IR spectro-photometric observations of our nearby AGN sample and interpret the observations with our 3D clumpy torus model (Hönig et al. 2006; Hönig & Kishimoto 2010). Details about the type 1 and type 2 sub-samples will be presented in Sect. 2. The observations and data reduction are described in Sect. 3. Section 4 discusses the results of the observations. In Sect. 5, we analyze the mid-IR characteristics of our sample and compare it to AGN properties. The data are then interpreted using our 3D clumpy torus model in Sect. 6. We summarize our main conclusions in Sect. 7.

2. Properties of the AGN sample

2.1. Sample selection

Our main goal is to obtain the highest spatial resolution spectro-photometric data set of AGN yet obtained in the mid-IR. Still, the sample cannot be considered “complete” in any respect, and restrictions and selection criteria are outlined below. We do consider the sample to be “typical” (or representative) though for the Seyfert galaxy population in the Galactic vicinity (see below). Moreover, it should give us an idea of the “clean” nuclear emission at scales of tens of parsecs.

The original idea for selecting objects was based on a demand of high-spatial resolution. In particular, we aimed for objects that have a resolution $< 100\ \text{pc}$ around $10\ \mu\text{m}$ using the 8.2 m UT3-telescope at Paranal. Thus, we are limited to AGN at angular-diameter distances $\leq 70\ \text{Mpc}$ ¹. Because the ESO/Paranal

observatory hosting VISIR is located in the Southern hemisphere, the whole sample is limited to objects mostly at Southern declinations. In addition, to facilitate observations in service mode, the AGN were selected to be brighter than 100 mJy in most of the *N*-band. Based on these criteria, we mined the AGN catalog of Veron-Cetty & Veron (2006) and compared the objects to previous low-spatial resolution mid-IR data from *Spitzer* and ISO to be able to estimate which objects are bright enough for VISIR. Since our ultimate goal concerns typical nearby AGN, i.e. Seyfert galaxies, all peculiar objects (e.g. LINERs) were skipped. To avoid synchrotron contamination, we also excluded radio-loud objects. Finally, because we are interested in the characteristics of the AGN, we avoided any objects where the nucleus is heavily obscured by host-galactic dust lanes, as e.g. in Circinus. Thus, any obscuration pattern seen in the data of most of our objects (i.e. silicate absorption features) is supposedly intrinsic to the nuclear environment. However, we acknowledge that IC 4329A and NGC 7582 have dust lanes passing over the nucleus, so that part of the observed absorption properties may originate in the host galaxy (in particular for the Seyfert 2 NGC 7582; see Sect. 6 for possible consequences on our analysis and modeling). In summary, we selected nine type 1 and ten type 2 AGN.

2.2. Observed and intrinsic scales

In Tables 1 and 2, we list the basic characteristics of our type 1 and type 2 AGN sub-sample. If the objects are Compton-thin, the intrinsic (absorption-corrected) 2–10 keV X-ray luminosity can serve as a proxy for the total luminosity of the AGN. For the type 1 AGN (see Table 1), we also provide optical luminosities, which are more direct tracers for the accretion disk luminosity. Observed scales for each object are provided at the reference wavelength of $8\ \mu\text{m}$.

Another way to look at our main requirement of high-spatial resolution is not the *observed* scale but the *intrinsic* scale of each object. Because most of the nuclear mid-IR radiation in radio-quiet Seyfert is presumably coming from dust emission, the fundamental scaling relation between the dust sublimation radius and the AGN luminosity, $r_{\text{sub}} \propto L^{1/2}$, provides such a distance-independent scaling. If we take UV/IR-reverberation mapping data (e.g. Suganuma et al. 2006, and references therein) and use the calibrated relation from Kishimoto et al. (2007), we obtain $r_{\text{sub}} = 0.36\ \text{pc} \times (L_V/10^{45}\ \text{erg/s})^{1/2}$. For the type 1 AGN, we can directly calculate the expected r_{sub} from their optical luminosity and compare r_{sub} to the spatial resolution of our observations (see Table 1). As can be seen, all of the objects that meet our resolution selection $< 100\ \text{pc}$ (corresponding to $D_L \leq 73\ \text{Mpc}$) have an *intrinsic* spatial resolution $< 2000\ r_{\text{sub}}$. Because the intrinsic scale is the ultimate factor determining how well the AGN can be isolated from the host galaxy, it is probably safe to include additional objects in the sample with a spatial resolution $> 100\ \text{pc}$, but still an intrinsic resolution $< 2000\ r_{\text{sub}}$ without compromising our goal of highest spatial resolution. Thus, we include Markarian 509, which adds to the higher luminosity end of the type 1 sub-sample.

Because the UV/optical emission from the accretion disk is thought to be obscured in type 2 AGN, a direct comparison between observed scales and intrinsic scales is not possible via the reverberation-based size-luminosity relation. However, based on our type 1 sub-sample, we are able to convert the size-luminosity relation from the optical to other wavebands. Because we are dealing with mid-IR observations, the most convenient

¹ Please note that the distances given in Tables 1 and 2 are *luminosity* distances D_L . The corresponding D_L to our 70 Mpc limit would be $D_L \leq 73\ \text{Mpc}$.

Table 1. Characteristics of our type 1 AGN mid-IR spectroscopic sample.

Object	Type ^a	z	D_L^b (Mpc)	log Luminosities (erg/s)				Object scales		
				L_X (N_H) ^c	L_V^d	$L_{[OIII]}^e$	$L_{12\mu m}^f$	r_{sub}^g (pc)	$8\mu m$ (pc) ^h	res. (r_{sub})
NGC 3227	S1.5	0.0049	20.4	42.40 (22.80)	42.20	40.51	42.63	0.014	24.2	1680
NGC 3783	S1.5	0.0108	44.7	43.19 (22.47)	42.98	41.30	43.57	0.035	52.5	1482
NGC 4593	S1.0	0.0101	42.0	42.89 (20.30)	42.88	40.69	43.18	0.032	49.5	1560
ESO 323–G77	S1.2	0.0159	66.3	42.76 (23.25)	43.91	41.05	43.75	0.104	77.1	741
MCG–6–30–15	S1.5	0.0087	35.8	42.86 (21.67)	43.41	40.36	43.09	0.058	42.3	727
IC 4329A	S1.2	0.0170	70.5	43.87 (21.65)	44.11	41.21	44.20	0.131	82.0	625
MARK 509	S1.5	0.0335	141	43.94 (20.70)	44.01	42.29	44.25	0.116	158	1365
NGC 7213	S1.5L	0.0051	21.2	42.33 (20.60)	42.76	39.87	42.50	0.028	25.2	913
NGC 7469	S1.5	0.0151	62.7	43.33 (20.61)	43.09	41.44	43.87	0.040	73.1	1808

Notes. ^(a) AGN types from Veron-Cetty & Veron (2006): S: Seyfert, L: LINER; ^(b) luminosity distance based on CMB reference frame redshifts from NED and $H_0 = 73$, $\Omega_m = 0.27$, and $\Omega_{vac} = 0.73$; ^(c) L_X = absorption-corrected 2–10 keV luminosity from Dadina (2007), except for NGC 3227 (Tueller et al. 2008), logarithmic intrinsic Hydrogen column densities N_H in units of cm^{-2} from Tueller et al. (2008), except ESO 323–G77 (average of Beckmann et al. 2006; Malizia et al. 2007); ^(d) $L_V \equiv \nu L_\nu(5500 \text{ \AA})$; from Bentz et al. (2009), except NGC 7213 (Winkler 1992), ESO 323–G77 (Schmid et al. 2003), and MCG–6–30–15 (Bennert et al. 2006). Additional extinction correction applied to IC 4329A and ESO 323–G77 (Winkler et al. 1992), and NGC 3783 ($A_V = 1.0$ from $H\alpha/H\beta$; de Grijp et al. 1992); ^(e) [O III] total line fluxes from Schmitt et al. (2003) (NGC 3783, NGC 4593, MCG–6–30–15, NGC 7213), Meléndez et al. (2008) (NGC 3227, IC 4329A, MARK 509, NGC 7469), and Schmid et al. (2003) (ESO 323–G77); ^(f) $L_{12\mu m} \equiv \nu L_\nu(12 \mu m)$; this work; ^(g) from the fit to K -band reverberation mapping data as shown in Kishimoto et al. (2007); observed $U - J$ or $U - K$ time lag radii: 0.071 pc (NGC 3783), 0.084 pc (MARK 509), 0.044 pc (NGC 7469); ^(h) spatial scale corresponding to the theoretical diffraction limit for a 8.2 m VLT telescope: $0''.25$ at $8 \mu m$, $0''.31$ at $10 \mu m$, $0''.37$ at $12 \mu m$.

Table 2. Characteristics of our type 2 AGN mid-IR spectroscopic sample.

Object	Type ^a	z	D_L^b (Mpc)	log Luminosities (erg/s)				Object scales		
				L_X (N_H) ^c	$L_{[OIII]}^d$	$L_{12\mu m}^e$	r_{sub}^f (pc)	$8\mu m$ (pc) ^g	res. (r_{sub})	
NGC 2110	S1i	0.0080	33.2	42.60 (22.57)	40.35	43.00	0.028	39.2	1392	
ESO 428–G14	S2	0.0063	26.0	... (>24)	40.62	42.73	0.020	30.8	1509	
MCG–5–23–16	S1i	0.0095	39.5	43.24 (22.47)	40.63	43.53	0.052	46.6	900	
NGC 4507	S1h	0.0128	53.0	43.34 (23.46)	41.57	43.69	0.062	62.1	1004	
MCG–3–34–64	S1h	0.0176	73.2	42.78 (23.69)	41.45	44.14	0.104	84.9	814	
NGC 5643	S2	0.0047	19.2	... (>24)	40.55	42.49	0.016	22.9	1471	
NGC 5995	S1.9	0.0257	107	43.52 (21.95)	42.01	44.06	0.095	122	1294	
IC 5063	S1h	0.0109	45.3	42.87 (23.28)	41.28	43.82	0.072	53.2	737	
NGC 7582	S1i	0.0044	18.3	42.04 (22.98)	40.15	42.71	0.020	21.8	1093	
NGC 7674	S1h	0.0277	116	43.72 (24.00)	41.93	44.26	0.120	132	1103	

Notes. ^(a) AGN types from Veron-Cetty & Veron (2006): S: Seyfert, L: LINER, S1i: optical type 2 with broad Hydrogen lines in the infrared; S1h: type 2 with detected polarized optical broad lines; ^(b) luminosity distance based on CMB reference frame redshifts from NED and $H_0 = 73$, $\Omega_m = 0.27$, and $\Omega_{vac} = 0.73$; ^(c) L_X = absorption-corrected 2–10 keV luminosity from Dadina (2007), except IC 5063 (Tueller et al. 2008), MCG–3–34–64 and NGC 4507 (Hönig et al. 2008a), NGC 5995 (Horst et al. 2008), and NGC 7674 (Bianchi et al. 2005); logarithmic intrinsic Hydrogen column densities in units of 10^{22} cm^{-2} from Tueller et al. (2008), except ESO 428–G14 (Della Ceca et al. 2008), NGC 5643 (Maiolino et al. 1998), and NGC 7674 (Bianchi et al. 2005, changing-look AGN); ^(d) [O III] fluxes from Schmitt et al. (2003) (NGC 4507, IC 5063, NGC 7674), Meléndez et al. (2008) (NGC 5643, NGC 7582), Gu et al. (2006) (ESO 428–G14, MCG–3–34–64), Haas et al. (2007) (NGC 2110), Winkler (1992) (MCG–5–23–16), and Tran (2003) (NGC 5995); ^(e) $L_{12\mu m} \equiv \nu L_\nu(12 \mu m)$; this work; ^(f) based on Eq. (1); ^(g) theoretical diffraction limit for a 8.2 m VLT telescope: $0''.25$ at $8 \mu m$, $0''.31$ at $10 \mu m$, $0''.37$ at $12 \mu m$.

way is a conversion of the size-luminosity relation to $12 \mu m$. This wavelength is mostly outside the silicate feature so that it is not affected by possible anisotropies due to silicate absorption or emission. Recent high-spatial resolution studies (also using the VISIR instrument on the 8.2-m VLT/UT3 telescope) have shown that type 1 and type 2 AGN follow basically the same $L_{MIR} - L_X$ -relation in the luminosity range as that covered by our sample (Horst et al. 2006, 2008; Gandhi et al. 2009). The anisotropy between the two samples is within the observational errors and is smaller than about a factor of 2 to 3. Thus, $L_{12\mu m}$ can also serve as a proxy for the AGN luminosity of our objects and enables us to estimate intrinsic scales. We note that this is only a good approximation as long as high spatial resolution data are available.

As a first step, we determine the correlation between L_V and $L_{12\mu m}$ in the type 1 sub-sample, assuming that the covering

factor is similar for all objects. We find that $\log L_V = (6.9 \pm 9.6) + (0.84 \pm 0.22) \times \log L_{12\mu m}$ (Spearman rank 0.88, null-hypothesis probability 5×10^{-3}). Within errors, this is consistent with $L_V \propto L_{12\mu m}$, with a ratio $L_V/L_{12\mu m} = 0.59^{+0.82}_{-0.34}$, which we assume below. With this correlation, we obtain a scaling relation for our AGN sample of

$$r_{sub} = (0.28^{+0.15}_{-0.10}) \text{ pc} \times \left(\frac{L_{12\mu m}}{10^{45} \text{ erg/s}} \right)^{1/2}. \quad (1)$$

Despite the uncertainty of a factor of 1.5, this should enable us to give at least an estimate of the intrinsic scales of our type 2 objects. The intrinsic scales based on Eq. (1) are given in Table 2. As can be seen, while NGC 5995 and NGC 7674 have observed scales >100 pc, their intrinsic scales are $<2000 r_{sub}$, even when accounting for the factor of 1.5 uncertainty in Eq. (1). These two

objects have been added to our sample to have higher luminosity Seyferts in both the type 1 and type 2 sub-samples. We note that the relation based on L_X instead of $L_{12\ \mu\text{m}}$ would not improve the results ($r_{\text{sub}} = 0.45^{+0.32}_{-0.18} \text{ pc} \times (L_X/10^{45} \text{ erg/s})^{1/2}$).

In summary, our objects can be described as a sample of typical nearby Seyfert galaxies – obscured and non-obscured – spanning the luminosity range from about 10^{42} erg/s to 10^{44} erg/s. The intrinsic spatial resolution achieved by our observations is $<2000 r_{\text{sub}}$. Please note that we accidentally included one optically broad-line (BL) LINER in our sample, NGC 7213 (allegedly a “type 1 LINER”), which will be treated as a type 1 AGN in the rest of the paper but discussed separately where applicable.

3. Observations and data reduction

3.1. Spectroscopy

We used the VISIR mid-infrared imager and spectrograph mounted on the 8.2 m UT3 telescope at the ESO/Paranal observatory in Chile. The observations were carried out in service mode in ESO periods 78, 80, 82, and 83. In total, nine Seyfert 1 and ten Seyfert 2 galaxies were observed in low-spectral (LR) resolution mode ($R \sim 300$). The standard configuration for LR long-slit spectroscopy results in a pixel resolution of $0''.127$, which samples the PSF in the N -band by ~ 2.5 pixels. To cover the full N -band, four different spectral settings have to be used with central wavelengths at $8.5\ \mu\text{m}$, $9.8\ \mu\text{m}$, $11.4\ \mu\text{m}$, and $12.4\ \mu\text{m}$. We used a slit width of $0''.75$ which is approximately 2–3 times larger than the $FWHM$ achieved with VISIR ($0''.25$ – $0''.39$ across the N -band) and minimizes the risk of slit losses. All of our targets are unresolved point-sources, except for NGC 7469 where some off-nuclear emission is expected from the circumnuclear star-burst ring.

For the initial steps of data reduction, we followed the standard ESO pipeline. The individual chopped nodding cycles (chopping width $8''$, nodding in parallel mode) were combined and wavelength-calibrated with the Common Pipeline Library (CPL) recipes in *ESOREX*. After that, we used our own procedures to calibrate and extract the spectra. First, the remaining sky-offset was removed. For that, we fitted a low-order polynomial in spatial direction to each wavelength bin (typically of orders 0 to 2). We note that this procedure can only be used because we are not interested in very large-scaled smooth structure – which would not be visible anyway because of the flux limit. This polynomial sky-subtraction flattened the image background significantly (see Fig. 1).

However, a periodic background pattern in spatial direction remained in each wavelength bin, with a frequency length of 16 pixels and not depending on chopping width, frequency, or position angle. In usual observing conditions, this pattern dominates the total variance of the background. The ratio of object peak to background variation peak can be as low as 4:1 in AGN, which is very disturbing when dealing with faint mid-IR objects. We developed an efficient method to remove this background pattern with a “periodic background map (PBM)”. The PBM is generated by creating a cube with several copies of the sky-removed science array, each copy shifted by 16 pixels in spatial direction with respect to the previous copy. Finally, all shifted science-array copies are combined by median-filtering each pixel. The resulting PBM contains only the 16-pixel-frequency background without flux from the (point-like or slightly resolved) science target. In Fig. 1, we illustrate

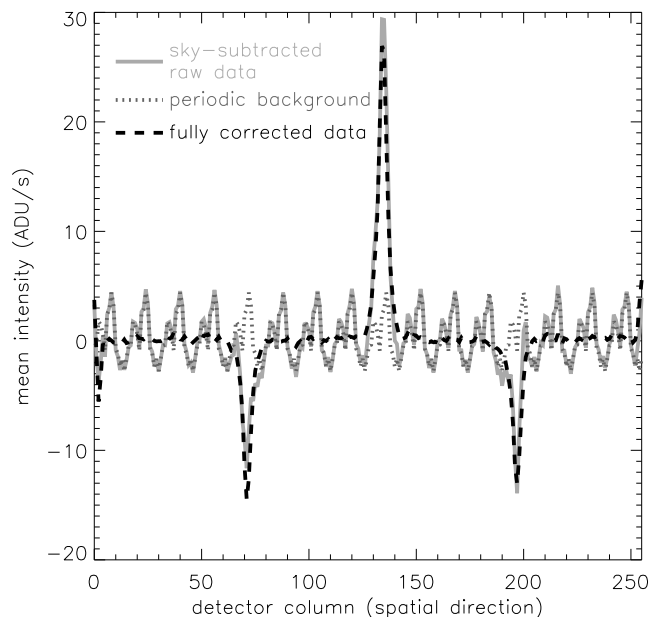


Fig. 1. Illustration of the periodic background map (PBM) removal for the $12.4\ \mu\text{m}$ setting of NGC 7213. The solid light-gray line represents the raw data after sky subtraction (mean over all rows). The PBM is shown by the dotted dark-gray line. The dashed black line presents the final data after PBM removal.

the PBM removal for the $12.4\ \mu\text{m}$ setting of NGC 7213. The solid light-gray line represents the raw data after sky subtraction (mean over all rows). For these data, the PBM has been determined as shown by the dotted dark-gray line. The dashed black line shows the final data after PBM removal. As can be seen, the noise variation is significantly suppressed as compared to the original data.

The described procedure was applied to both science and calibrator data. After removing all background, wavelength-dependent conversion factors were determined from the calibrators and the science data were flux-calibrated accordingly. We refrained from airmass corrections because the differential airmasses between target and calibrator were rather small, so that corrections would be within the calibration errors. For MCG–3–34–64, we found a beam-centering problem. In fact, visual inspection of acquisition images revealed that only part of the object was placed within the $0''.75$ slit. We used the acquisition images in the N_{SW} filter (made through the open slit) of the science target and the calibrator to quantify the loss due to this problem. The measured flux for MCG–3–34–64 in this filter is $F(N_{\text{SW}}) = 421.06 \pm 24.75$ mJy (wavelength: $8.85 \pm 1.35\ \mu\text{m}$). Compared to the integrated flux in the spectrum, we found that only about $70 \pm 4\%$ of the object flux was located within the slit. Thus, we corrected the flux-calibrated spectra of MCG–3–34–64 accordingly.

3.2. Imaging photometry

Along with the spectroscopy data, we acquired VISIR images in several mid-infrared filters to compare and validate the absolute and relative flux calibration of our spectra. Together with archival VISIR data, all of our objects were observed in at least two different narrow-band filters between $8\ \mu\text{m}$ and $13\ \mu\text{m}$, except for NGC 7674 (only one filter). For photometry, the standard CPL pipeline products were used for both science target and calibrator. The imaging was performed in parallel or

Table 3. VISIR mid-IR photometry of our nine type 1 AGN measured by Gaussian fitting to science target and calibrators.

Object	Filter name	λ_c (μm)	$\Delta\lambda$ (μm)	Flux (mJy)	$FWHM$ target/calib	Observing date
NGC 3227	ArIII	8.99	0.14	179.6 ± 11.3	0'32/0'31	2008-03-22T02:37
	PAH2ref2	11.88	0.37	320.1 ± 21.9	0'37/0'33	2008-03-22T02:41
NGC 3783	PAH1	8.59	0.42	323.9 ± 33.7	0'31/0'26	2008-03-20T06:08
	ArIII	8.99	0.14	350.9 ± 23.2	0'30/0'29	2008-03-20T06:16
	SIV	10.49	0.16	558.4 ± 23.2	0'31/0'31	2005-04-17T01:27
	PAH2ref2	11.88	0.37	595.8 ± 39.2	0'34/0'32	2008-03-20T06:20
	NeIIref1	12.27	0.18	685.0 ± 37.2	0'35/0'32	2005-04-17T01:36
NGC 4593	ArIII	8.99	0.14	181.8 ± 13.8	0'31/0'26	2008-04-01T06:32
	PAH2ref2	11.88	0.37	278.8 ± 20.4	0'36/0'31	2008-04-01T06:35
ESO 323-G77	ArIII	8.99	0.14	298.9 ± 11.5	0'40/0'29	2009-05-19T00:58
	PAH2ref2	11.88	0.37	377.4 ± 7.6	0'37/0'36	2009-05-10T01:01
MCG-6-30-15	SIV	10.49	0.16	311.7 ± 11.4	0'32/0'38	2006-04-14T03:58
	PAH2	11.25	0.59	359.6 ± 24.7	0'33/0'33	2006-04-14T04:03
	NeIIref1	12.27	0.18	377.5 ± 11.2	0'36/0'36	2006-04-14T04:07
IC 4329A	ArIII	8.99	0.14	743.4 ± 22.0	0'30/0'29	2009-05-19T01:12
	PAH2ref2	11.88	0.37	1014.1 ± 18.8	0'36/0'36	2009-05-10T01:15
MARK 509	SIV	10.49	0.19	207.3 ± 17.0	0'35/0'34	2006-06-14T10:20
	PAH2	11.25	0.59	240.8 ± 27.1	0'32/0'32	2006-06-14T10:25
	NeII	12.81	0.21	243.0 ± 19.8	0'30/0'35	2006-06-14T10:30
NGC 7213	SIV	10.49	0.16	239.1 ± 22.0	0'33/0'32	2006-07-14T09:58
	PAH2	11.25	0.59	273.3 ± 34.5	0'37/0'34	2006-07-14T10:03
	NeIIref1	12.27	0.18	245.6 ± 16.9	0'35/0'32	2006-07-14T10:07
NGC 7469	SIV	10.49	0.16	447.8 ± 15.6	0'39/0'31	2006-07-12T07:21
	PAH2	11.25	0.59	470.1 ± 38.8	0'42/0'34	2006-07-12T07:25
	PAH2ref2	11.88	0.37	505.9 ± 25.4	0'34/0'32	2006-07-14T09:29
	NeIIref1	12.27	0.18	595.0 ± 18.0	0'36/0'34	2006-07-12T07:30
	NeIIref2	13.04	0.22	629.7 ± 16.6	0'35/0'47	2008-08-26T06:48

Notes. If several calibrators were available, the fluxes and $FWHM$ are mean values.

perpendicular chop/nod mode, so that three or four beams appear on the detector for the science data (parallel: two negative single-beams and one positive double-beam). On the other hand, the standard stars were observed almost exclusively in perpendicular chop/nod mode resulting in four single-beams (two negative, two positive beams).

Each science and calibrator beam was fitted by a two-dimensional Gaussian to resemble the core of the Airy disk of the PSF. We confirmed that our science targets are point sources in the mid-IR by comparing the Gaussian width of the targets with the standard stars. The measured Gaussian $FWHM$ of science target and associated calibrator² are given in Table 3. Although the science targets usually have slightly larger $FWHM$ than the calibrators, the differences are not significant except for MCG-3-34-64 and IC 5063, which we will discuss in Sect. 5.1 in detail. In most cases, the differences between the $FWHM$ of the science targets and calibrators are probably the result of PSF instabilities of VISIR, which are known to be a common problem (Horst et al. 2009). Therefore we consider that our sources are mostly unresolved. After the Gaussians were removed, all science targets showed the first Airy ring without any additional emission source except for NGC 7469. This galaxy has a well-known nuclear star-burst ring within 2'' of the nucleus which we spatially resolved in our observations and which contains more flux than the first Airy ring.

The final fluxes were obtained by calculating conversion factors from the integrated intensity of the Gaussian fits of the calibrators and using these factors for the respective integrated Gaussian intensity of the science targets. Because we are only

² Where several calibrators were available, the given calibrator $FWHM$ is the average of all calibrators.

interested in point source fluxes, this method of optimized extraction has the advantage that any flux from off-nuclear emission is excluded. This provides the best possible estimate for the torus emission, which is presumably unresolved. The resulting fluxes are presented in Tables 3 and 4. All data were obtained with a chop throw of 8'', except for the archival PAH2ref2 filter data of NGC 7469 and the archival NeIIref2 filter data of MCG-3-34-64, where a chop throw of 10'' was used.

4. Results and discussion

4.1. VISIR spectra and photometry

In Figs. 2 and 3 we show the individual VISIR 8–13 μm spectra of our type 1 AGN (eight Seyfert galaxies and one BL LINER) together with results from VISIR photometry. In the lower-right corner of each panel, we note the slit position angle (PA) for each object. The corresponding data of the ten Seyfert 2 galaxies are shown in Fig. 4. In addition to these data, the corresponding *Spitzer* IRS low-resolution spectra are shown for the same wavelength range. The spatial resolution of the IRS spectra is $\sim 3''$, while the VISIR data resolves scales of $\sim 0'.3$ at 10 μm . For NGC 7582, no *Spitzer* spectrum was available yet. The positions of prominent emission lines seen in AGN are shown. The gray-hatched areas in each spectrum mark regions of extensive skyline emission/absorption, which are difficult to calibrate due to some degree of variability within the night and/or compromised S/N ratios.

All VISIR spectra (except MCG-5-23-16; see below) have lower or equal fluxes than the *Spitzer* spectra, which is expected for the higher spatial resolution. A similar result for VISIR photometry on a sample of type 1 and type 2 AGN has recently

Table 4. VISIR mid-IR photometry of our ten type 2 AGN measured by Gaussian fitting to science target and calibrators.

Object	Filter name	λ_c (μm)	$\Delta\lambda$ (μm)	Flux (mJy)	<i>FWHM</i> target/calib	Observing date
NGC 2110	PAH1	8.59	0.42	156.6 ± 9.9	0'33/0'32	2006-10-10T07:28
	ArIII	8.99	0.14	169.1 ± 6.4	0'31/0'29	2006-10-10T07:31
	PAH2ref2	11.88	0.37	294.3 ± 8.0	0'33/0'35	2006-10-10T07:40
ESO 428-G14	PAH1	8.59	0.42	112.7 ± 18.5	0'37/0'41	2007-03-01T03:27
	ArIII	8.99	0.14	122.8 ± 14.4	0'40/0'30	2007-03-01T03:34
	PAH2ref2	11.88	0.37	207.1 ± 9.4	0'43/0'32	2007-03-01T03:42
MCG-3-34-64	SIV	10.49	0.16	591.9 ± 22.4	0'39/0'25	2006-04-09T05:23
	PAH2	11.25	0.59	685.8 ± 51.0	0'43/0'31	2006-04-09T05:31
	NeIIref1	12.27	0.18	889.3 ± 21.2	0'44/0'34	2006-04-09T05:35
	NeIIref2	13.04	0.22	1116.0 ± 60.7	0'46/0'36	2006-01-18T07:58
NGC 4507	SIV	10.49	0.16	489.2 ± 43.3	0'32/0'32	2006-04-15T02:58
	PAH2	11.25	0.59	554.7 ± 43.6	0'32/0'33	2006-04-15T03:02
	NeIIref1	12.27	0.18	631.4 ± 10.8	0'34/0'34	2006-04-15T03:07
MCG-5-23-16	PAH1	8.59	0.42	337.2 ± 10.5	0'27/0'33	2007-01-30T06:09
	ArIII	8.99	0.14	358.2 ± 16.7	0'28/0'32	2007-01-30T06:32
	PAH2ref2	11.88	0.37	633.4 ± 24.0	0'33/0'35	2007-01-30T06:40
NGC 5643	ArIII	8.99	0.14	143.3 ± 33.5	0'35/0'27	2009-05-03T04:58
	PAH2ref2	11.88	0.37	287.1 ± 9.1	0'37/0'35	2009-05-03T05:01
NGC 5995	SIV	10.49	0.16	266.0 ± 10.7	0'37/0'38	2006-04-14T04:48
	PAH2	11.25	0.59	332.5 ± 17.7	0'38/0'31	2006-04-14T04:52
	NeII	12.81	0.21	381.8 ± 20.2	0'40/0'33	2006-04-14T04:57
IC 5063	SIV	10.49	0.16	608.6 ± 22.0	0'47/0'37	2006-05-05T09:54
	PAH2	11.25	0.59	726.6 ± 24.7	0'43/0'38	2006-05-05T09:59
	PAH2ref2	11.88	0.37	924.9 ± 25.0	0'42/0'38	2005-06-10T08:06
	NeIIref1	12.27	0.18	1036.5 ± 56.2	0'43/0'37	2006-05-05T10:03
NGC 7582	PAH1	8.59	0.42	327.2 ± 37.7	0'51/0'41	2008-08-18T09:29
	ArIII	8.99	0.14	235.9 ± 27.2	0'33/0'29	2008-08-23T08:41
	PAH2ref2	11.88	0.37	383.6 ± 26.2	0'38/0'33	2008-08-23T08:38
NGC 7674	NeII	12.81	0.21	518.4 ± 21.7	0'45/0'38	2006-07-13T08:55

Notes. If calibrators were available, the fluxes and *FWHM* are mean values.

been reported by Horst et al. (2009). Together with the fact that the imaging-photometry is well consistent with the spectrophotometry, this confirms the self-consistency of the extracted fluxes and supports the consistency of our calibration approach with respect to other observations.

In MCG-5-23-16 the VISIR spectrum is slightly above both the Spitzer spectrum and the VISIR photometry data point. Because the VISIR photometry matches the Spitzer fluxes we account this discrepancy to some unknown calibration error in spectroscopy (e.g. a slightly deviating spectral shape of the calibrator). In the extreme case around 12 μm , the difference is 50 mJy or 7% of the flux. In NGC 7469, the VISIR photometry is slightly but systematically lower the VISIR spectrum. The reason for this is that the extraction window used for the spectroscopic data includes some small degree of emission from the surrounding star-burst ring (see also Sect. 4.2 and Horst et al. 2009) while our optimal flux extraction for imaging isolated the nuclear point source.

As most ground-based mid-IR instruments, VISIR uses chopping and nodding to subtract the strong sky emission. But this procedure does not only affect the background, it also has an influence on the science data: if an emission region is extended on scales larger than the chop-throw, this emission is strongly reduced. The degree of suppression depends on the actual extension and spatial flux gradient. It is strongest for objects that are emitting light more or less uniformly. On the other hand, point-like objects or emission regions confined within the chop-throw are not affected. Thus chopping can be considered a useful

tool to reduce or suppress extended host galaxy emission. This contribution from the host galaxy can be stellar light or emission from extended star-formation projected onto the nucleus, in particular if the host galaxy is strongly inclined. In conclusion, our spectra and photometry can be expected to be free of extended host galaxy emission, containing only emission from the point-like AGN and its immediate vicinity.

4.2. Polycyclic aromatic hydrocarbon (PAH) emission and star-formation activity around the AGN

Thirteen of the *Spitzer* IRS spectra of our objects show more or less pronounced PAH emission features at 11.3 μm , and in some cases the 7.7/8.6 μm PAH complex is also well visible. Because PAH emission is associated with star-formation, these features in the IRS data indicate that star-formation is occurring in the central $\sim 3''$ of the AGN or, due to the lack of chopping, is projected onto the nucleus in the Spitzer data. Common to all of our high-spatial resolution VISIR spectra as compared to the *Spitzer* IRS data is the lack, or at least strong suppression, of PAH line emission. Most objects do not display any 11.3 μm PAH emission, while in NGC 3227, NGC 5643, NGC 5995, NGC 7469, and NGC 7582 some minor PAH feature can be seen. For Mrk 509 the situation is inconclusive due to the low quality of the 12.4 μm setting, and for NGC 4593 we do not have data in the corresponding spectral setting. In the cases with some little 11.3 μm PAH emission, it is difficult to judge if some marginally remaining feature at around 8.6 μm is also present

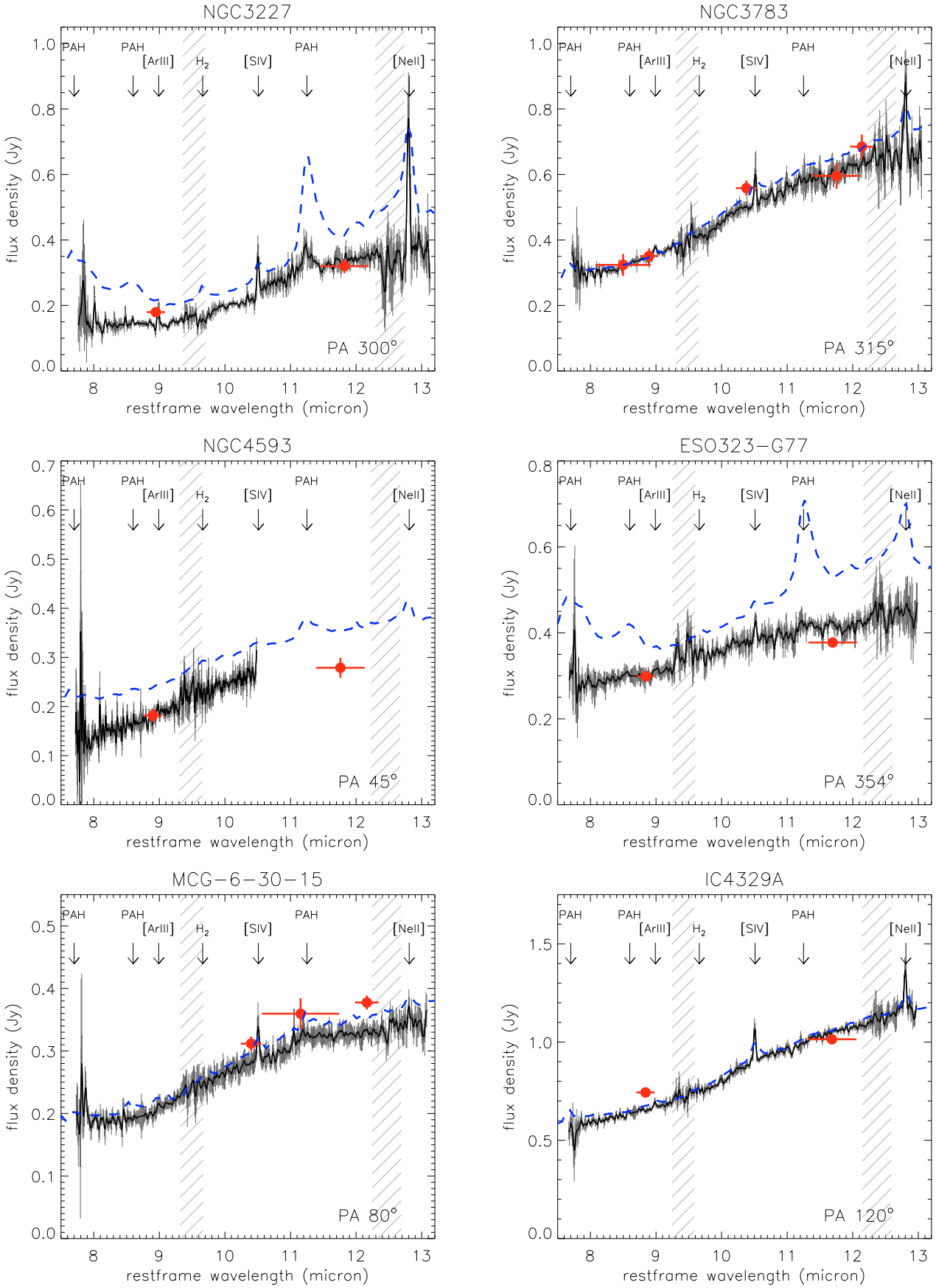


Fig. 2. VISIR low-resolution spectroscopy (black solid line and gray error bars) and photometry (red filled circles) of eight type 1 AGN. Overplotted (blue dashed line) are Spitzer data with approximately 10 times less spatial resolution. The hatched areas mark regions with strong sky lines, which are difficult to calibrate. Prominent mid-IR emission line positions are indicated. The slit position angle (PA) is given in the lower right corner of each panel.

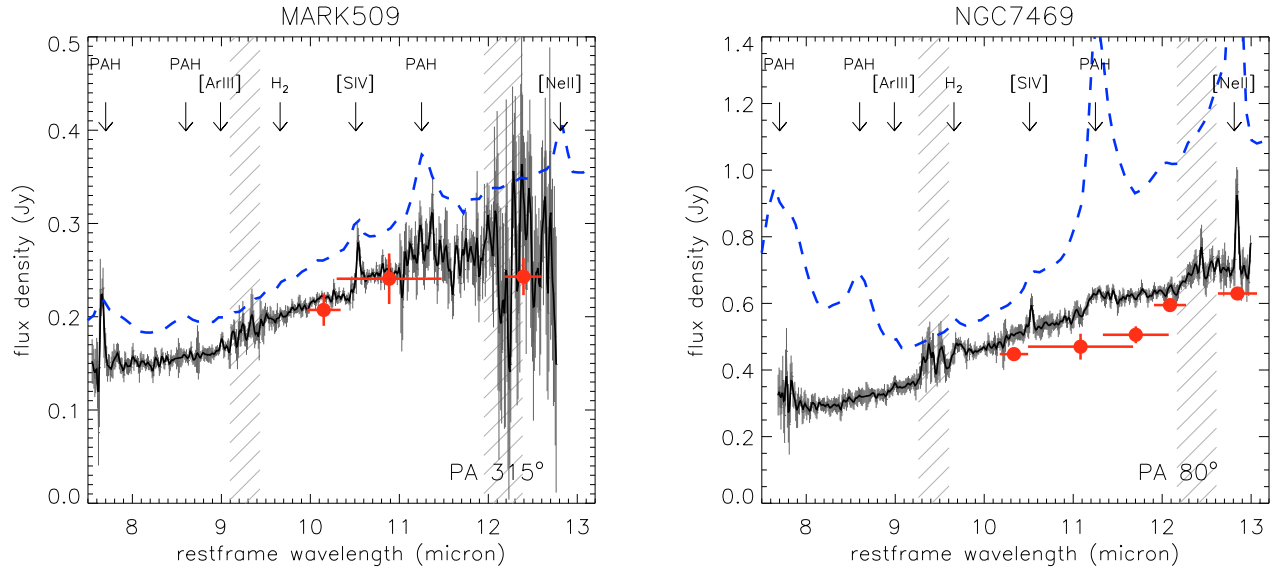


Fig. 2. continued.

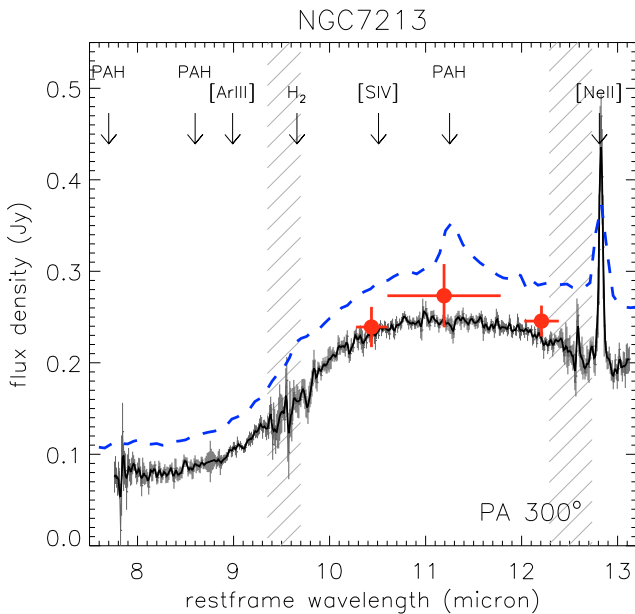


Fig. 3. VISIR low-resolution spectroscopy (black solid line and gray error bars) and photometry (red filled circles) of the LINER galaxy NGC 7213. Overplotted (blue dashed line) are Spitzer data with approximately 10 times less spatial resolution. The hatched areas mark regions with strong sky lines, which are difficult to calibrate. Prominent mid-IR emission line positions are indicated. The slit position angle (PA) is given in the lower right corner.

(e.g. by comparing to the Spitzer data), given that this feature is generally broader in wavelength and weaker. It has to be pointed out that the suppression of the PAH emission features is not an effect of different *spectral* resolution, but is only caused by the different *spatial* resolution and observing techniques.

In Fig. 5 we show examples of IRS minus VISIR differential spectra of objects with prominent PAH emission in the IRS spectra, NGC 3227, NGC 5643 and NGC 7469. For that, the VISIR data were downgraded to the same spectral resolution as IRS ($R \sim 100$). The differential spectra were compared to the scaled-down version of the IRS spectrum of M 82

(blue-dashed line), which is often used as an extragalactic star-formation template. The match for all three sources is reasonably good, especially for NGC 7469. Thus we conclude that the differential spectra from spatial regions between $\sim 0''.3$ – $3''$ are predominantly showing star-formation emission in the continuum and lines.

The main differences of spectra taken with *Spitzer* and VISIR are spatial resolution and observing technique. Because our spatial resolution is about a factor of 10 better than the IRS data, the emission regions producing the PAH features can simply be located at scales between $0''.3$ and $3''$. On the other hand, only in few cases individual star-forming regions are actually seen in the VISIR images, and images of these cases were recently shown by Horst et al. (2009). The most notable example is NGC 7469 with its well-known star-burst ring at about $2''$ from the nucleus. When integrating over a $0''.75 \times 3''$ aperture, we recovered part of the IRS spectrum. The remaining “missing flux” probably originates from extended emission outside the VISIR aperture or from the host galaxy projected onto the nucleus. Because VISIR uses the chopping/nodding technique, any extended host galaxy emission at scales beyond the chop throw will be eliminated from the data or, at least, significantly reduced. As a result, the nuclear point source flux is free of contaminating emission from the host galaxy, even if part of the host emission falls onto the nucleus.

Still, most of the PAH emission in Spitzer is supposed to come from the vicinity of the AGN. Because we selected galaxies with only moderate inclination, projection effects should play a minor role. Consequently we see a significant reduction of the PAH emission from scales of 1 kpc down to <100 pc. What is the reason for the suppression of the PAH emission features? The PAH dust grains are prone to photo-destruction by high-energetic photons as emitted by an AGN or in its vicinity (e.g. from hot thermal plasma). Therefore it is quite plausible that they become less abundant at smaller distances from the AGN. On the other hand, a lack of PAH emission can also point to reduced or no star-formation activity. While it is not possible to distinguish between both effects only from the PAH emission, the reduction of PAH emission features from IRS to VISIR goes along with a reduction in continuum flux in our spectra. If the only reason for suppressed PAH emission were

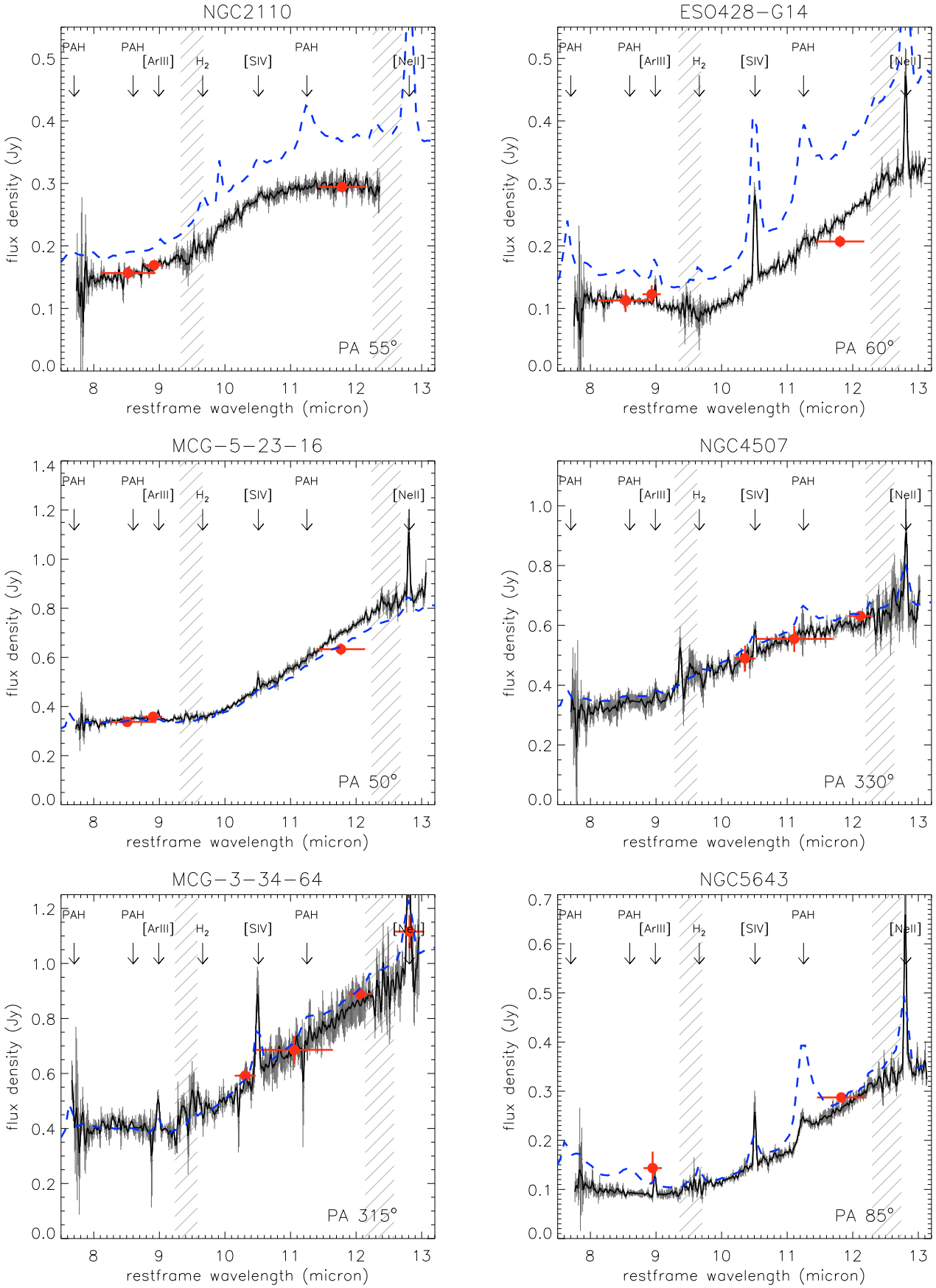


Fig. 4. VISIR low-resolution spectroscopy (black solid line and gray error bars) and photometry (red filled circles) of ten type 2 AGN. Overplotted (blue dashed line) are Spitzer data with approximately 10 times less spatial resolution. The hatched areas mark regions with strong sky lines, which are difficult to calibrate. Prominent mid-IR emission line positions are indicated. The slit position angle (PA) is given in the lower right corner of each panel.

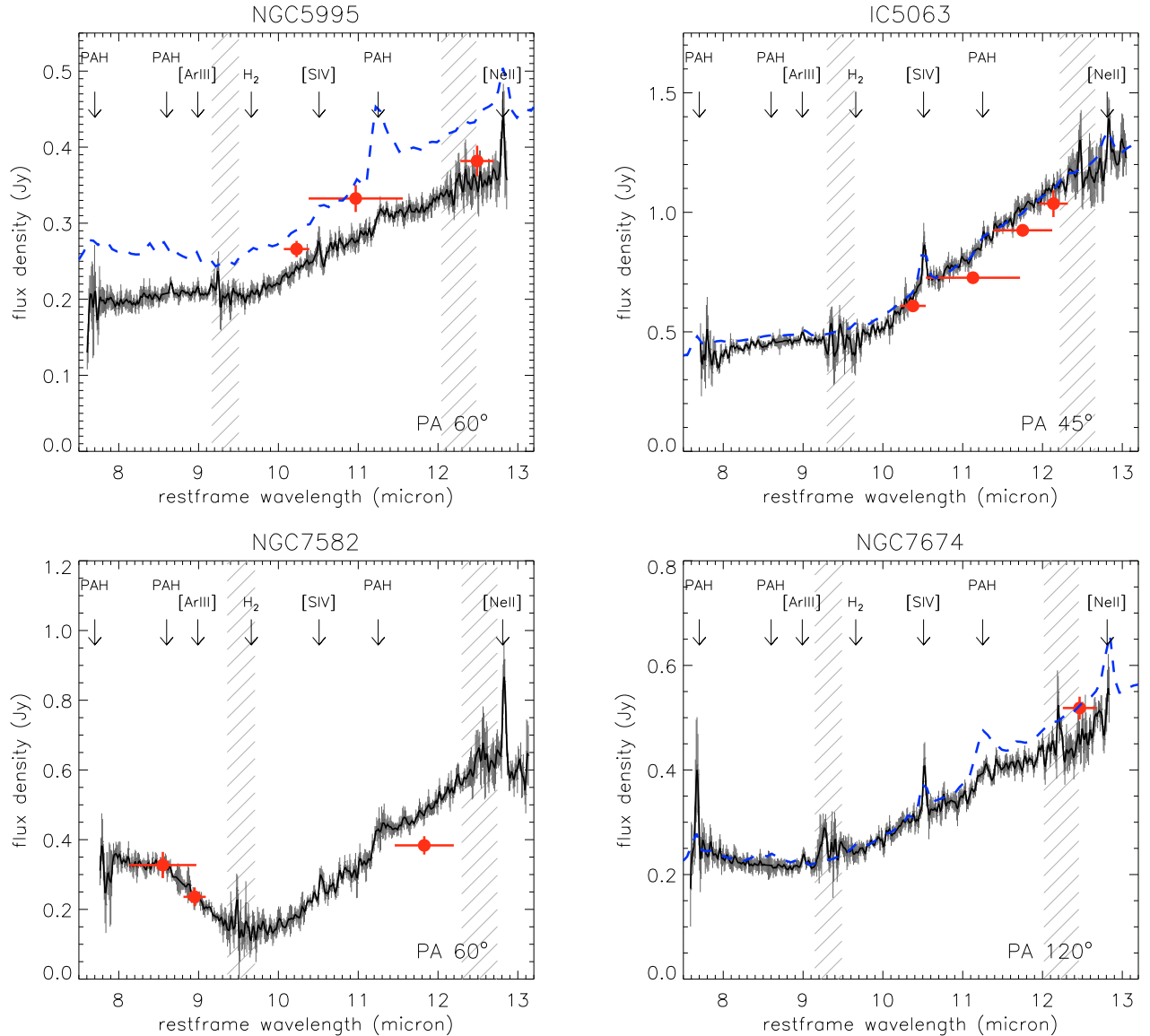


Fig. 4. continued.

photo-destruction of the associated grains, we expect that the continuum level remains roughly constant. Thus we conclude that the dominating effect of suppressed PAH emission is an actual decrease in star-formation activity at smaller distances from the AGN.

4.3. The *N*-band silicate feature in AGN at high spatial resolution

Silicate absorption and emission features are the most evident spectral signatures in the *N*-band. One of the surprising discoveries of *Spitzer* was based on observations of silicate emission features in type 1 AGN. The features were much weaker than expected from early torus modeling (e.g. Pier & Krolik 1993; Granato & Danese 1994; Efstathiou & Rowan-Robinson 1995). The same also holds for silicate features in absorption as seen in type 2 AGN, although very deep features are sometimes seen in ULIRGs or type 2 AGN, where the host galaxy presumably contributes by a large fraction to the obscuration (e.g. Levenson et al. 2007; Polletta et al. 2008; Martinez-Sansigre et al. 2009).

Because the *Spitzer* data have a spatial resolution of several arcseconds in the *N*-band, it was not clear initially to what degree the weakness of the silicate features was a resolution effect. Recent ground-based mid-IR spectroscopy of single objects at high spatial resolution suggested however that even at a resolution better than 1'' silicate absorption and emission features were moderate (e.g. Roche et al. 2007; Mason et al. 2009). Here we present a much larger sample of type 1 and type 2 AGN observed at sub-arcsecond resolution so that the silicate feature characteristics can be studied more systematically (see Sect. 5.3).

Figure 2 illustrates that most type 1 AGN exhibit a rather weak emission feature, if we can detect any at all. A small bump in the continuum can be seen somewhere between 9 μm and 12 μm e.g. in NGC 3783 and MCG-6-30-15. The other features are only revealed when plotting $\log \nu F_\nu$, or fitting the continuum (see Sect. 5.3) and some seem to be *absorption* rather than emission features (e.g. NGC 3227). The strongest silicate emission feature is displayed by the weak or LINER AGN NGC 7213 (Fig. 3). Based on the spatial resolution of our data of <100 pc in all objects except MARK 509, we conclude that the weakness

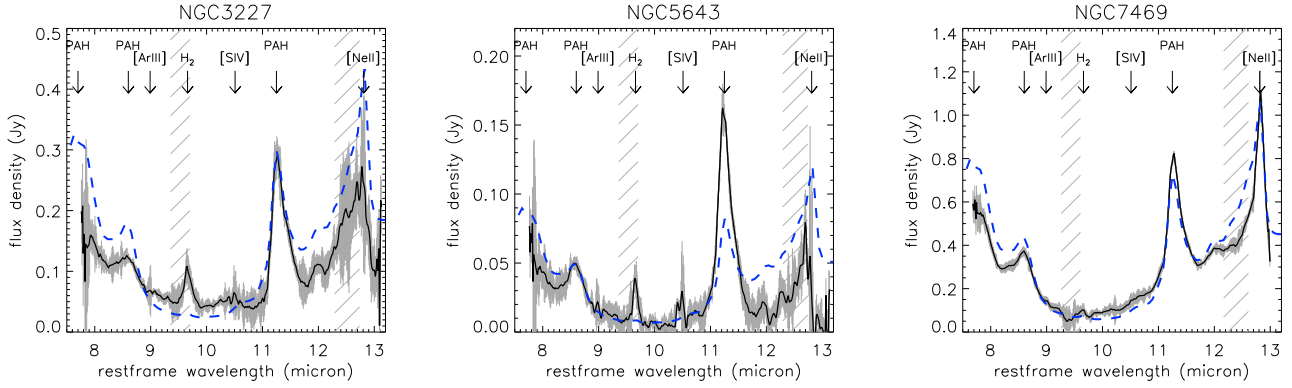


Fig. 5. *Spitzer* IRS minus VISIR differential spectra of NGC 3227 (left), NGC 5643 (middle), and NGC 7469 (right). The differential spectra are compared to the scaled-down IRS spectrum of M 82 (blue-dashed line), which is commonly used as a template for extragalactic star-formation.

of the silicate emission features in type 1 AGN is not a spatial resolution effect, but an intrinsic property of the features and possibly of the emission region.

The type 2 AGN show a variety of feature characteristics (see Fig. 4). While most type 2s have moderate silicate features in absorption, the NGC 4507 *N*-band spectrum resembles a featureless type 1 spectrum. In NGC 2110 we even see the silicate feature in emission. It is not surprising to see these different characteristics in type 2s because we expect various torus inclinations realized in these objects, ranging from moderate to very high obscuration (“edge-grazing” to edge-on geometries). This is illustrated by the variety of Hydrogen column densities N_{H} observed in X-rays for these AGN (see Table 2). Indeed NGC 2110 has the lowest N_{H} within the type 2 sub-sample, and infrared broad emission lines were reported (Veron-Cetty & Veron 2006) (see Mason et al. 2009, for possible scenarios in NGC 2110).

One of the mysteries of the silicate feature in AGN is an actual or apparent shift of the emission feature towards longer wavelengths. Absorption features in type 2 AGN are centered very close to $9.7 \mu\text{m}$, just as expected from opacity curves of the Galactic ISM dust (Chiar & Tielens 2006). Clumpy torus models based on ISM dust well reproduce the overall IR dust re-emission and the silicate absorption features in detail (e.g. Hönig et al. 2006, 2007; Polletta et al. 2008; Schartmann et al. 2008). For type 1 AGN, the situation is less clear. Early reports of the silicate emission feature in a number of quasars discussed that the central wavelength might be shifted towards longer wavelengths (Hao et al. 2005; Siebenmorgen et al. 2005; Sturm et al. 2005). Recently Nikutta et al. (2009) suggested that radiative transfer effects might cause the silicate emission feature in AGN to shift towards longer wavelengths. In their analysis, they require a certain number of clouds to intervene the line-of-sight of other clouds to cause some absorption dip at the center of the silicate feature. To occur at the right wavelength, they suggest using Ossenkopf et al. (1992) silicates with a peak wavelength at $10.0 \mu\text{m}$ instead of standard ISM. However, they note that any slightly larger number of clouds or different opacity would cause a noticeable absorption dip to be present in the center of the silicate emission feature, as shown in the models of Nenkova et al. (2008) and Hönig & Kishimoto (2010). Based on our own modeling, we would expect that if these radiative transfer effects are the *only* reason for a shift or the silicate emission feature, we expect that analyzing a sample of objects would reveal both shifted features and those showing noticeable absorption dips within the emission feature. However, all the type 1 AGN observed here and in addition NGC 2110 as a type 2 AGN with a

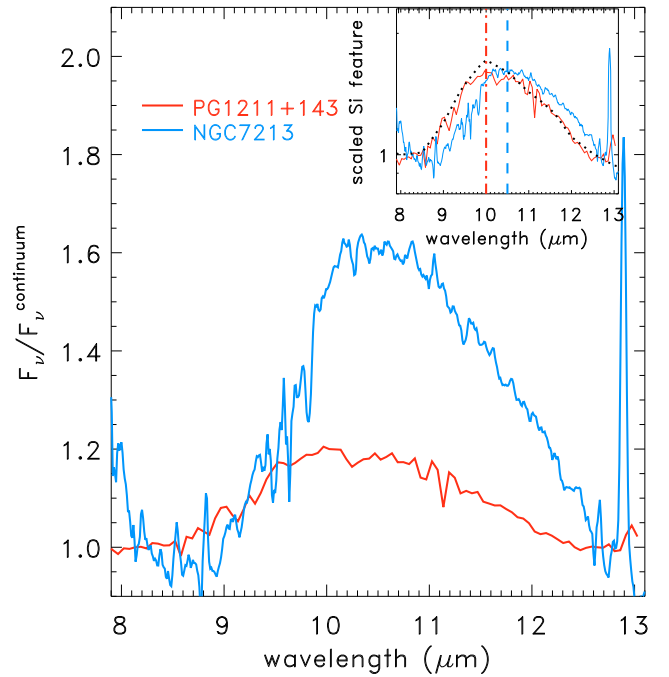


Fig. 6. Continuum-normalized silicate emission features of PG1211+143 (red) and NGC 7213 (blue). A linear continuum was fitted to both objects based on their $8.3 \mu\text{m}$ and $12.7 \mu\text{m}$ fluxes and the observed spectrum was divided by this continuum fit. The small inset shows both features in log plot normalized for their different feature strengths. As a comparison we overplot the extinction coefficient of standard ISM dust with Ossenkopf silicates (black-dotted line). The blue-dashed and red-dotted-dashed lines denote the central wavelengths of NGC 7213 and PG 1211+143 respectively.

silicate emission feature do *not* show this absorption dip within the emission feature. This is consistent with a detailed study of the silicate emission features of 23 PG quasars observed with *Spitzer* (Schweitzer et al. 2008). The problem was also mentioned by Mason et al. (2009) when attempting to model the silicate emission feature in NGC 2110. In addition, we note that our modeling of silicate features with Ossenkopf et al. silicate opacities shows both emission *and* absorption features centered at $10.0 \mu\text{m}$, in agreement with Nenkova et al. (2008). Because the observed absorption feature central wavelength is at $9.7 \mu\text{m}$ though (see also Mason et al. 2006; Roche et al. 2007; Hönig et al. 2007), type 2 AGN would favor different opacity curves.

In Fig. 6 we show a comparison between the continuum-normalized N -band *Spitzer* spectrum of PG 1211+143 analyzed by Nikutta et al. (2009) and our VISIR spectrum of NGC 7213. To estimate the continuum, we made a linear fit to the $8.3 \mu\text{m}$ and $12.7 \mu\text{m}$ fluxes in F_ν . The observed spectra were then divided by the continuum fit. With this kind of fit (which is to some extent similar to the method suggested by Sirocky et al. 2008; and used by Nikutta et al. 2009), we see that the peak emission of PG 1211+143 is indeed located at $10.0 \mu\text{m}$, while it is shifted to $\sim 10.5 \mu\text{m}$ in NGC 7213. We compared these features to the extinction curve of standard ISM dust with Ossenkopf silicates and found that the PG 1211+143 silicate emission profile is well matched, while a shift is evident in NGC 7213. Note that if we used the *Spitzer* IRS spectrum of NGC 7213 instead of the VISIR spectrum, the result would be more or less the same.

In summary we conclude that simple radiative transfer effects due to absorption within the torus *alone*, either clumpy or smooth, are not capable of explaining the details of the silicate features and their characteristics in type 1 and type 2 AGN. There may be other effects contributing to the actual shape of the feature. One possibility is that there is some (radial) change of the grain size and/or dust composition based on the fact that large grains, preferably graphite grains, have a much higher sublimation temperature than smaller grains, in particular silicates. Then hotter regions might be dominated by graphite dust and larger grains, while cooler regions have an ISM-like size and graphite-silicate mix, which may go along with a temperature-dependent central wavelength of the silicate feature (e.g. as illustrated in Krügel 2008, Fig. 9.7). Consequently, exact details on absorption and emission within the silicate feature are more complex than covered by recent torus models, although the essence of the features (i.e. feature strength) is well captured by these models.

5. AGN continuum and dust emission properties in the mid-IR at <100 pc

As shown in the previous section, the high-spatial resolution of VISIR allows us to isolate the nuclear mid-IR emission in AGN without too much disturbance from host-galactic sources. Thus an analysis of these data will reveal characteristics of the circumnuclear region around the AGN. Below we will discuss several properties of the mid-IR continuum emission and the silicate features. Narrow forbidden atomic emission lines that are also present in the spectra like [Ar III], [S IV], and [Ne II] were already studied in part in Hönig et al. (2008a), and the whole sample will be dealt with separately in an upcoming paper.

5.1. Mid-IR continuum emission and its relation to AGN luminosity tracers

The mid-IR emission is believed to originate from dust reprocessing of the central accretion disk radiation. In particular, optical/UV photons hit the dust in the torus and heat up the grains. The absorbed energy is then re-emitted in the IR and forms the general IR bump seen in multi-wavelength SEDs (e.g. Elvis et al. 1994). This redistribution of energy should produce a fairly significant correlation between the X-ray (accretion disk tracer) and mid-IR (dust emission tracer) luminosity in AGN. A $L_{\text{MIR}} - L_X$ -correlation has been found by several authors using both space-based and ground-based observations (e.g. Krabbe et al. 2001; Lutz et al. 2004; Horst et al. 2008; Gandhi et al. 2009). One remarkable property of this correlation is the apparent isotropy among the AGN: Within the observational scatter

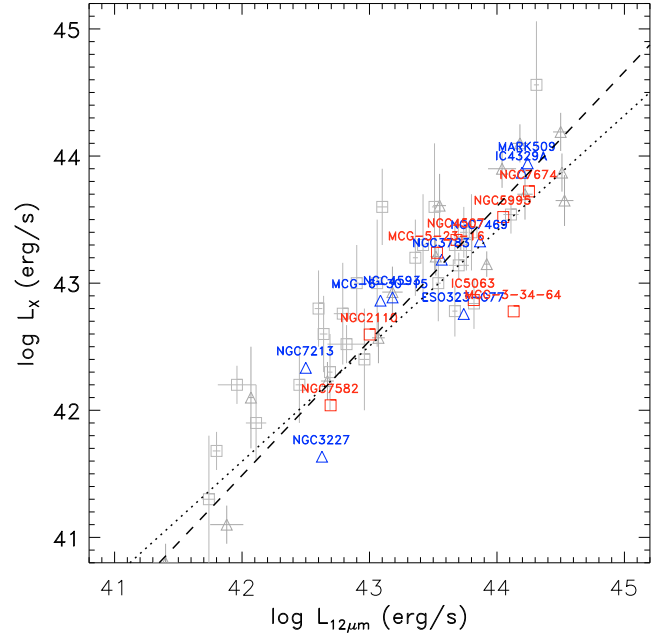


Fig. 7. Absorption-corrected X-ray luminosities L_X of our sample of AGN plotted against the $12 \mu\text{m}$ luminosity $L_{12 \mu\text{m}}$ derived from the VISIR spectra, excluding Compton-thick objects (see Tables 1 and 2). The blue triangles are type 1 objects, while the red squares are type 2 AGN. The dotted line is the best-fit correlation for our whole sample, while the dashed line represents a fit to the sample excluding the outliers (see Sect. 5.1) The gray symbols show the full sample of the latest version of the $L_{\text{MIR}} - L_X$ -correlation as presented in Gandhi et al. (2009).

of the latest version of the correlation of about a factor of 2 to 3 (Gandhi et al. 2009), there seems to be no difference between type 1 and type 2 AGN.

In Fig. 7 we show the absorption-corrected X-ray luminosities L_X of our sample of AGN plotted against the $12 \mu\text{m}$ luminosity $L_{12 \mu\text{m}}$ derived from the VISIR spectra (see Tables 1 and 2). Compton-thick objects are not shown in the plot. The errors of the mid-IR luminosities are < 0.1 dex (typical photometric accuracy is much better than 15%). The X-ray luminosities are taken from single-epoch data, so that we consider typical uncertainties in L_X due to intrinsic variability of ~ 0.5 dex (see error of the Gandhi et al. 2009, sample overplotted as gray symbols in Fig. 7). Within the scatter of our observations, there is no apparent difference between type 1 and type 2 AGN. This is consistent with the larger samples analyzed by Horst et al. (2008) and Gandhi et al. (2009); the latter sample is shown for comparison as gray symbols in Fig. 7. Note that some objects in the original Gandhi et al. sample are duplicated in our sample. However, different X-ray luminosities were used and the mid-IR fluxes were extracted from our VISIR spectra. Using our much smaller sample leads to a nominal correlation $L_{12 \mu\text{m}} \propto L_X^{1.06 \pm 0.15}$ (Spearman rank $\rho_{\text{Spearman}} = 0.82$, null-hypothesis probability 4.9×10^{-5}), which is consistent with the findings in Gandhi et al. (2009). There seems to be a small offset of our sample towards lower mid-IR luminosities with respect to the Gandhi et al. study. This can be explained to a small degree by the fact that Gandhi et al. used $12.3 \mu\text{m}$ as the reference wavelength, where fluxes are usually slightly higher than at $12.0 \mu\text{m}$ as used here. Most of the difference comes from the method used to extract the fluxes though: our photometry was measured using the optimal extraction, while in Gandhi et al. (2009) aperture photometry was used, which potentially includes some off-nuclear emission.

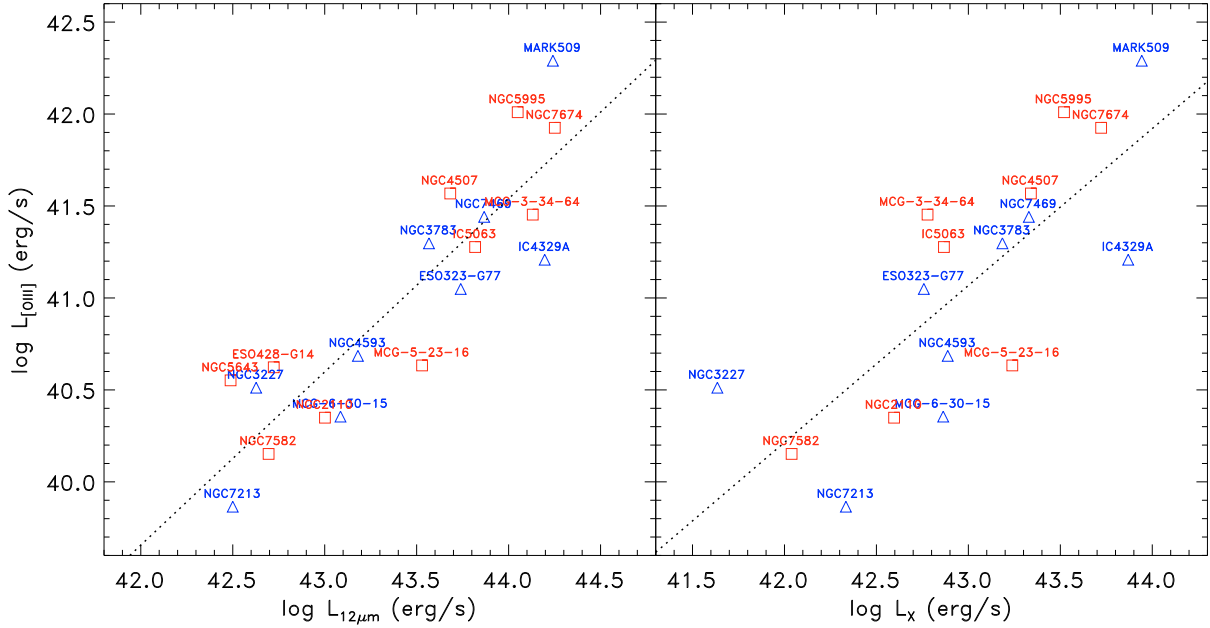


Fig. 8. [O III] luminosities of our sample compared to the $12\ \mu\text{m}$ mid-IR (left) and 2–10 keV X-ray luminosities. The blue triangles are type 1 AGN, the red squares denote type 2 objects. The dotted lines are best-fit correlations for the whole sample (left: $L_{[\text{O III}]} \propto L_{12\ \mu\text{m}}^{0.96 \pm 0.12}$; right: $L_{[\text{O III}]} \propto L_X^{0.85 \pm 0.18}$).

The non-detection of a difference between type 1 and type 2 AGN within the error of observations might indicate a relatively large degree of isotropy of the AGN radiation in both the mid-IR and the X-ray. However, it has to be noted that the $L_{\text{MIR}} - L_X$ -correlation omits all Compton-thick objects. Unless one has a good idea of the intrinsic X-ray luminosity of these highly obscured objects (e.g. from line emission at optically thin wavelengths as in Hönig et al. 2008a), the observed isotropy must be considered as a lower limit. One such possibility is the commonly used [O III] ($\lambda 5007\ \text{\AA}$) luminosity, although some degree of anisotropy has been reported (e.g. Netzer et al. 2006). In Fig. 8 we compare the [O III] luminosities of our sample to the $12\ \mu\text{m}$ mid-IR and 2–10 keV X-ray luminosities, respectively. Both properties correlate well with $L_{[\text{O III}]}$, but the $L_{12\ \mu\text{m}} - L_{[\text{O III}]}$ -relation is stronger by eye and by a statistical analysis. For our sample we find $\log L_{[\text{O III}]} = (0.11 \pm 5.3) + (0.94 \pm 0.12) \times \log L_{12\ \mu\text{m}}$ (Spearman rank $\rho = 0.87$, null-hypothesis probability 1.3×10^{-6}) and $\log L_{[\text{O III}]} = (4.38 \pm 7.8) + (0.85 \pm 0.18) \times \log L_X$ (Spearman rank $\rho = 0.78$, null-hypothesis probability 1.9×10^{-4}). Note that for the correlation with $L_{12\ \mu\text{m}}$, there are also Compton-thick objects included (NGC 5643 and ESO 428–G14). Thus, if the [O III] radiation is considered as being a good isotropy tracer, then $L_{12\ \mu\text{m}}$ may be considered as being emitted quite isotropically as well – at least more isotropically than X-ray radiation. This might also be interpreted as a sign that the mid-IR optical depth of any obscuring medium (e.g. as traced by the X-ray hydrogen column density N_{H}) must be more transparent in the mid-IR, or that the mid-IR emission is emitted within or outside the X-ray-opaque medium.

These findings seem to have a natural interpretation in the unification scheme: the dusty torus is both the X-ray-obscuring and the mid-IR-emitting medium. Recent studies showed that the observed mid-IR isotropy (i.e. small dispersion between type 1 and type 2 AGN in the $L_{\text{MIR}} - L_X$ -correlation) can be explained within the framework of a clumpy torus (e.g. Hönig et al. 2006; Horst et al. 2008; Nenkova et al. 2008; Gandhi et al. 2009; Levenson et al. 2009). There is an interesting point to consider

though: While IC 5063, ESO 323–G77, and MCG–3–34–64 are outliers in the $L_{\text{MIR}} - L_X$ -correlation (see Fig. 7 and also Horst et al. 2008; Gandhi et al. 2009), they are very close to the $L_{12\ \mu\text{m}} - L_{[\text{O III}]}$ -fit (see Fig. 8). This could be caused by absorption because all three objects have moderate N_{H} ($\log N_{\text{H}} \sim 23$). On the other hand, all recent $L_{\text{MIR}} - L_X$ -studies use N_{H} -corrected L_X so that it is difficult to imagine that the intrinsic L_X are still underestimated by a factor of ~ 3 –5. Another possibility would be that these objects are not “underluminous” in the X-rays but “overluminous” in the mid-IR, i.e. there is additional mid-IR emission other than the dust torus re-emission. This overhead emission is probably triggered by the AGN, because our spectra do not include any major star-burst component (see Sect. 4.2). Instead the additional mid-IR emission may originate from dust in the narrow-line region (NLR). The prime example for this is NGC 1068. Mason et al. (2006) point out that the flux in the central $1''2$ of this AGN ($\sim 80\ \text{pc}$, which is a typical resolution element of our sample) contains only 30% contribution from the nuclear point source (presumably the torus) while 70% originate in extended emission, mostly from the NLR³. This corresponds to a mid-IR “overluminosity” of 0.3–0.4 dex in the $L_{\text{MIR}} - L_X$ -correlation, which is about the offset of the three sources. If we exclude these sources from the $L_{\text{MIR}} - L_X$ -correlation analysis, we obtain a tight relation of $L_{12\ \mu\text{m}} \propto L_X^{0.94 \pm 0.10}$ (Spearman rank $\rho_{\text{Spearman}} = 0.96$, null-hypothesis probability 2.5×10^{-8}), which is consistent within errors with Gandhi et al. (2009).

An interesting aspect about this suggestion is that mid-IR VISIR imaging of the outliers MCG–3–34–64 and IC 5063 actually shows extended emission. Horst et al. (2009) mention some “slight elongation” in their SIV, PAH2, and NeII_1 filter images of MCG–3–34–64, but attribute it to instrumental effects. We reanalyzed their images of MCG–3–34–64 and IC 5063, together with additional archival VISIR images (see Fig. 9), by

³ We note that the NGC 1068 data used in Figs. 10 to 12 are point source values from a $0''.4$ extraction window.

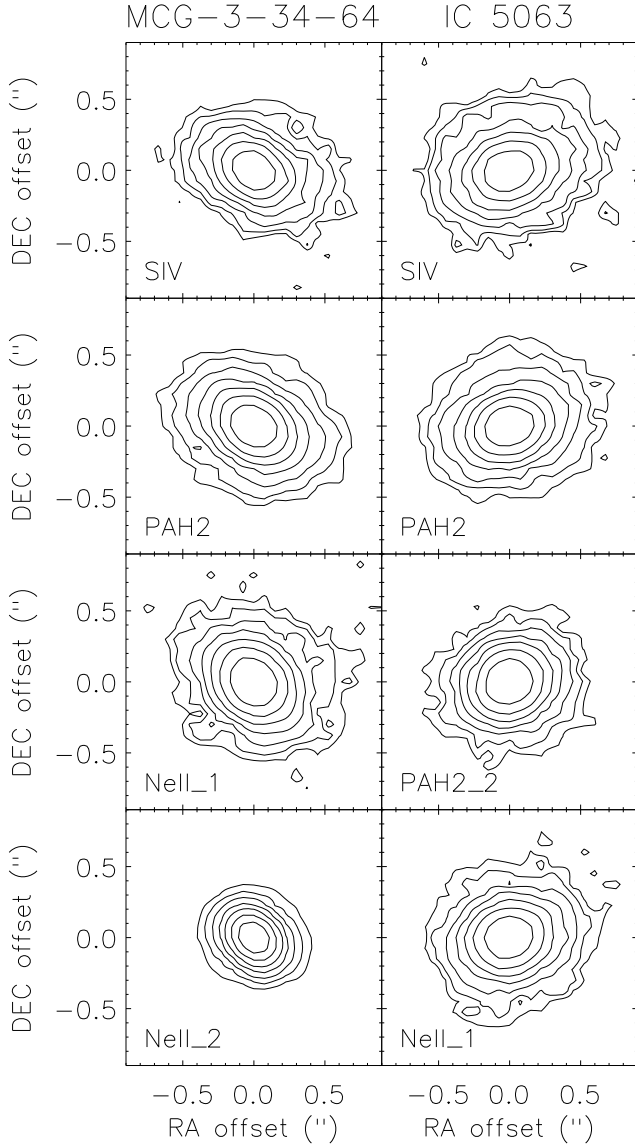


Fig. 9. VISIR mid-IR contour images of MCG-3-34-64 (left column) and IC 5063 (right column). The different panels in each column represent images in different filters (SIV = forbidden [SIV](10.51 μm) line, PAH2 = 11.3 μm PAH line, PAH2_2 = 11.88 μm continuum, NeII_1 = 12.27 μm continuum, NeII_2 = 13.04 μm continuum). Contour levels are scaled logarithmically from the peak in steps of 0.2 dex down to the 4% peak flux level. Both objects show clear elongations, corresponding geometric properties based on Gaussian fits as listed in Table 5.

applying a 2D Gaussian fit to both science target and calibrator. The resulting $FWHM$ and position angles are presented in Table 5. The source MCG-3-34-64 shows at least 38–54% and IC 5063 shows at least 14–45% extension compared to the maximum elongation of the respective calibrators. All calibrators appear more or less round with axis ratios close to unity. On the other hand, the average axis ratios are 1.35 for MCG-3-34-64 and 1.26 for IC 5063. This agrees with very similar position angles in each filter while the orientation of the axis in the standard star images is more random (average PA 54° for MCG-3-34-64 and 111° for IC 5063). In IC 5063 this is consistent with the orientation of the extended [O III] emission as observed with HST (PA 115°; Schmitt et al. 2003). Even though no high-spatial resolution [O III] image is available for MCG-3-34-64,

Table 5. Gaussian fit geometric properties of MCG-3-34-64 and IC 5063 based on VISIR images.

Filter	Object properties		Calibrator properties	
	size	PA	size	PA
MCG-3-34-64				
SIV	0′.488 × 0′.342	59°	0′.316 × 0′.298	95°
PAH2	0′.514 × 0′.367	57°	0′.355 × 0′.320	93°
NeIIref1	0′.505 × 0′.400	45°	0′.365 × 0′.328	82°
NeIIref2	0′.562 × 0′.435	46°	0′.391 × 0′.384	129°
IC 5063				
SIV	0′.551 × 0′.417	110°	0′.380 × 0′.373	175°
PAH2	0′.508 × 0′.382	109°	0′.379 × 0′.368	69°
PAH2ref2	0′.452 × 0′.394	117°	0′.397 × 0′.385	36°
NeIIref1	0′.485 × 0′.394	107°	0′.384 × 0′.380	160°

we can compare our results to radio observations. Schmitt et al. (2001) report linear extension of the nuclear radio emission (inner ~ 100 pc) at 8.46 GHz towards PA 39°, which is only about 13° off from the mean elongation of the mid-IR emission. If we assume that the linear radio emission traces some jet-like emission and that the jet-like emission is approximately in the same direction as the NLR, we can argue that the mid-IR emission in MCG-3-34-64 is also extended in the NLR direction.

Actually, these two objects are the only ones in our sample where we see such a significant extension and elongation (see data in Tables 3 and 4; point-like images for some of our objects are shown in Horst et al. 2009). Moreover, some members of our group attempted VLTI/MIDI mid-IR interferometry on both objects in the past. Although total fluxes were easily recorded, no fringes were found. This is consistent with a very low 12 μm visibility (0.2–0.3 at about 60 m baselines) in these objects, meaning that 70–80% of the nuclear flux comes from extended emission. Thus based on (1) the absence of PAH emission lines in our VISIR spectra; (2) the resolved emission regions observed in the mid-IR images of MCG-3-34-64 and IC 5063; (3) the significant elongation; (4) consistent position angles of the mid-IR extended emission region and the [O III] emission in IC 5063 and the linear radio emission in MCG-3-34-64; and (5) the low visibilities in mid-IR interferometry, we suggest a scenario where these two objects have very mid-IR-bright NLRs – similar to NGC 1068 – which causes them to deviate from the $L_{\text{MIR}} - L_X$ -correlation. Whether or not this may also be an explanation for the apparent “overluminosity” of AGN at the low-luminosity end of the $L_{\text{MIR}} - L_X$ -correlation (Horst et al. 2008; Gandhi et al. 2009) has to be addressed by detailed mid-IR studies.

5.2. The mid-IR spectral index

One fundamental observational property of the mid-IR emission is its spectral slope. Because a sizable part of the N -band is affected by the silicate feature, the continuum slope has to be recovered from wavelengths outside the feature, which is centered around 10 μm . Here we assume that fluxes at 8.5 μm and 12.5 μm are mostly unaffected by the silicate feature (which we tested by inspecting ISM dust extinction curves and *Spitzer* IRS data covering a larger wavelength range).

In Fig. 10 we show the spectral slopes (=flux ratios $F_{\nu}(12.5 \mu\text{m})/F_{\nu}(8.5 \mu\text{m})$) and spectral indices $F_{\nu} \propto \nu^{\alpha}$ (based on the flux ratios) for all our objects. In the left panel we plot the spectral slope $\log F_{\nu}(12.5 \mu\text{m})/F_{\nu}(8.5 \mu\text{m})$ against the observed mid-IR luminosity. The distribution is rather wide, so that a clear correlation cannot be seen. Yet there may be a slight trend that

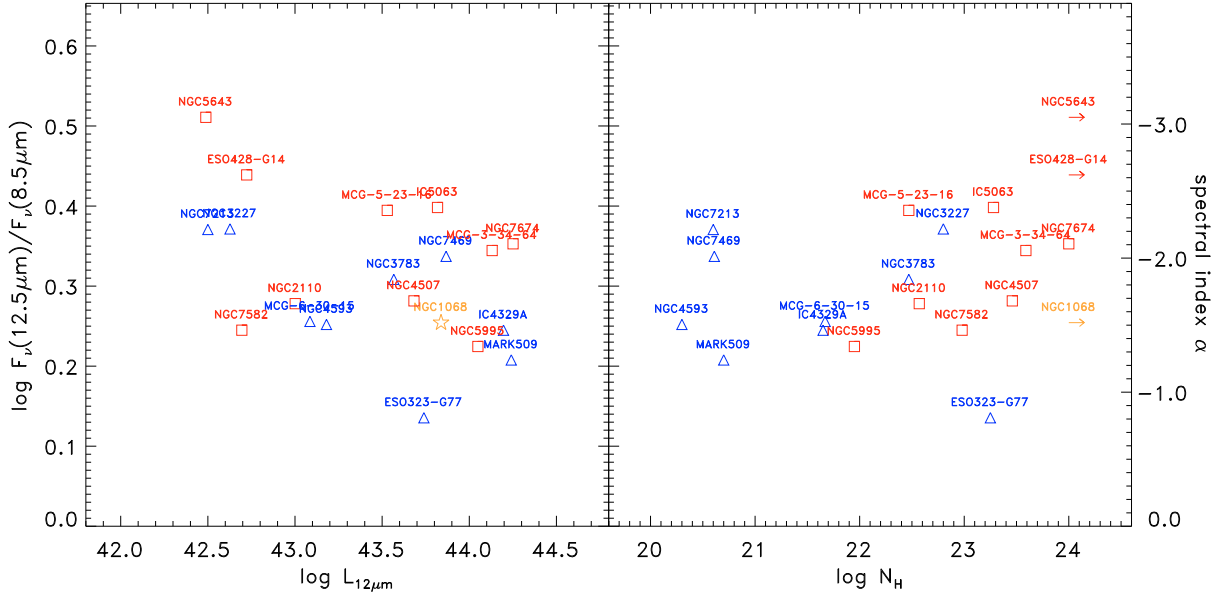


Fig. 10. Mid-IR spectral slope and spectral index for each object in our sample, plotted against the observed mid-IR luminosity $L_{12\ \mu\text{m}}$ and the X-ray Hydrogen column density N_{H} . Type 1 AGN are shown as blue triangles, type 2 objects are marked by red squares. For reference, NGC 1068 is shown as an orange star, based on the mid-IR spectrum from Mason et al. (2006).

the reddest objects in both the type 1 and type 2 sub-sample are on the lower luminosity end of the plot. What can clearly be seen is that type 1 and type 2 AGN do not show a huge difference in the spectral index α , i.e. type 1s can be as red as type 2 AGN, although a marginal difference may be detected. The nominal mean spectral indices are $\alpha_{\text{AGN1}} = -1.65 \pm 0.44$ for type 1 AGN and $\alpha_{\text{AGN2}} = -2.07 \pm 0.54$ for type 2 AGN. This almost similarity in spectral indices becomes even more evident when comparing the hydrogen column density N_{H} with the spectral index. There is at best a marginal trend of the spectral index with obscuration towards the AGN – the most obscured objects appear to be redder than the mean in this sample. On the other hand, NGC 1068 as a Compton-thick object has $\alpha = -1.5$ in the mid-IR, so that it is placed in the bulk of the other objects (see star in Fig. 10, left). The spectral index for each object has been tabulated in Table 6.

That type 1 and type 2 AGN have very similar spectral indices may seem quite surprising. The first-order assumption based on the torus picture would be that type 1 AGN are on average bluer than type 2 AGN, because most of the IR emission we see in type 1s comes from hot dust in the inner part of the torus. On the other hand, as shown in Hönig & Kishimoto (2010, e.g. Sects. 3.2, 3.4 and 3.5.1, and Figs. 6, 7, 9, 10, 11 and 12), the way the dust is distributed around the AGN can have a much stronger effect on the mid-IR properties than the inclination effects – in particular if the torus is clumpy so that transitions in obscuration properties from type 1 to type 2 are smooth. We demonstrated that if the radial dust distribution is steep ($\eta_r \propto r^a$ with $a = -1.5 \dots -2.0$), i.e. most of the dust is confined to small radii, the resulting SEDs are quite blue in both type 1 and type 2 orientations of the torus (see Hönig & Kishimoto 2010, , Figs. 6 and 9). On the other hand, more shallow dust distributions ($a = -0.5 \dots -1.0$) show redder colors for all orientations. Thus in the framework of a clumpy torus, the similarity in mid-IR spectral indices can be naturally explained. A larger difference in spectral indices may however emerge at wavelengths shorter than $8\ \mu\text{m}$.

Table 6. Properties of the VISIR mid-IR spectra.

Object	α	$\log F_{\text{Si}}/F_{\text{c}}$	τ_{silicate}
NGC 1068	-1.52	-0.16	0.38
NGC 2110	-1.66	0.01	-0.03
ESO 428-G14	-2.62	-0.25	0.57
MCG-5-23-16	-2.36	-0.14	0.32
NGC 3227	-2.22	-0.06	0.13
NGC 3783	-1.84	-0.03	0.06
NGC 4507	-1.68	0.02	-0.05
NGC 4593	-1.51	0.06	-0.15
ESO 323-G77	-0.81	0.02	-0.05
MCG-3-34-64	-2.06	-0.09	0.20
MCG-6-30-15	-1.53	0.03	-0.08
IC 4329A	-1.46	-0.01	0.02
NGC 5643	-3.05	-0.20	0.45
NGC 5995	-1.34	-0.05	0.13
MARK 509	-1.24	0.11	-0.25
IC 5063	-2.38	-0.12	0.28
NGC 7213	-2.21	0.10	-0.23
NGC 7582	-1.46	-0.45	1.03
NGC 7469	-2.01	0.01	-0.02
NGC 7674	-2.11	-0.08	0.19

Notes. For each object we list the 8.5–12.5 μm spectral index α , the silicate feature strength $F_{\text{Si}}/F_{\text{c}}$, and the corresponding optical depth in the silicate feature τ_{silicate} (see Sects. 5.2 and 5.3 for details).

5.3. The silicate feature and its relation to AGN properties

In Sect. 4.3 we qualitatively discussed the general appearance of silicate features at high spatial resolution. Now we aim for a quantitative analysis of the silicate feature and its relation to other observed properties. For that we fitted a linear continuum to the 8.5 μm and 12.5 μm flux of each object. From that we interpolate the expected linear continuum flux F_{c} at 9.8 μm around the center of the silicate feature (but see Sect. 4.3 for details on the central wavelength). Then we took the ratio between

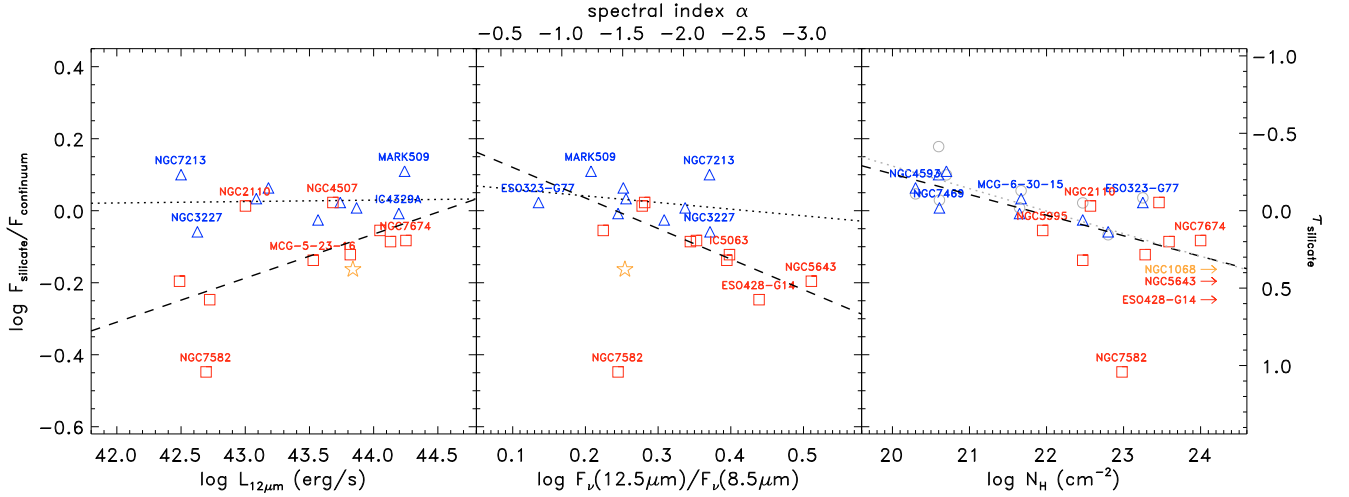


Fig. 11. Silicate feature analysis of our AGN sample observed with VISIR. Type 1 AGN are shown as blue triangles, type 2 AGN are marked by red squares. Some objects have been identified by name. For reference we include NGC 1068 with mid-IR properties based on the Gemini spectrum by [Mason et al. \(2006\)](#). *Left:* dependence of the silicate feature strength F_{Si}/F_c (see text for details) on the mid-IR luminosity $L_{12\ \mu\text{m}}$. The dashed line shows the nominal relation for type 2 AGN, the dotted line is the corresponding relation for type 1s. *Middle:* F_{Si}/F_c plotted against the spectral slope and spectral index of the mid-IR continuum emission. The dashed line shows the nominal relation for type 2 AGN, the dotted line is the corresponding relation for type 1s. *Right:* F_{Si}/F_c and observed optical depth in the silicate feature τ_{silicate} shown as a function of the Hydrogen column density N_{H} . The dashed line represents the correlation $F_{\text{Si}}/F_c \propto 0.12 \times \log N_{\text{H}}$. Gray circles are type 1 data points if the central wavelength of the silicate emission feature is $10.3\ \mu\text{m}$ instead of $9.8\ \mu\text{m}$. The corresponding correlation $F_{\text{Si}}/F_c \propto 0.14 \times \log N_{\text{H}}$ is shown as a dotted line.

observed flux and fitted continuum flux, F_{Si}/F_c , as a measure of the strength of the silicate feature, which is similar to the strategy used by [Hao et al. \(2007\)](#). The silicate feature strength of each object is listed in Table 6.

Figure 11 shows the silicate strength plotted against several observed parameters. The right axis shows the translation into an observed optical depth, τ_{silicate} , within the silicate feature. It has to be pointed out though that this does not reflect the actual optical depth along the line-of-sight towards the central engine, but is a result of the radiative transfer within the torus (see also [Hönig & Kishimoto 2010](#)). In the left panel, we show the silicate strength as a function of mid-IR luminosity $L_{12\ \mu\text{m}}$. As in all plots, the type 1 AGN are marked by blue triangles, and red squares are used for type 2 AGN. For reference, we put NGC 1068 in all of the plots based on the Gemini spectrum of the nucleus reported in [Mason et al. \(2006\)](#). The type 1 AGN are all clustered around $\log F_{\text{Si}}/F_c = 0$, reflecting the absence or extremely shallow silicate features. They do not show any dependence of the silicate feature on $L_{12\ \mu\text{m}}$ in the covered luminosity, with a nominal relation $\log F_{\text{Si}}/F_c \propto (0.00 \pm 0.03) \times \log L_{12\ \mu\text{m}}$ (dotted line in the left panel of Fig. 11). The type 2 AGN show a much larger variety of silicate feature strengths from moderate absorption to slight emission, as seen also in Fig. 4. The deepest feature is observed in NGC 7582. This galaxy shows a well-known star-burst ring close to the nucleus which is at high inclination (e.g. [Wold & Galliano 2006](#)). It seems quite likely that a large fraction of the obscuration in this object is not intrinsic to the torus but caused by dust located in or around the star-burst ring or the inner host galaxy. In general the silicate absorption features seem to become shallower with luminosity in the type 2 AGN. The dashed line in the left panel of Fig. 11 is the nominal fit to the type 2 sub-sample, $\log F_{\text{Si}}/F_c \propto (0.12 \pm 0.06) \times \log L_{12\ \mu\text{m}}$. We would not call this a correlation (Spearman rank $\rho = 0.58$, null-hypothesis probability 8.2×10^{-2}), but the data suggest at least that the silicate feature shows stronger differences between type 1 and type 2 AGN at lower than at higher luminosities. If this is really

true, it indicates that the dust distribution properties like the radial dust distribution or the average number of clouds along the equatorial line-of-sight (see [Hönig & Kishimoto 2010](#), for more details) may change with luminosity. This would agree with the possible trend of bluer spectral indices for higher luminosity objects mentioned in Sect. 5.2. Based on the discussions in [Hönig & Kishimoto \(2010\)](#), it is possible that higher luminosity AGN either have a more compact dust distribution (see also [Polletta et al. 2008](#)) or have less obscuring clouds in the torus (e.g. see [Hönig & Beckert 2007](#)). Follow-up studies on a more substantial sample and luminosity range should be done to further investigate these trends. We will continue this discussion in Sect. 6.3.

A fundamental prediction of all kinds of torus models is that line-of-sight obscuration, spectral color and silicate feature are correlated. As a first-order approximation, we expect that the SEDs of type 2 AGN are slightly redder than type 1 AGN. If we have a face-on view onto the torus, the near-to-mid-IR SED is dominated by hot-dust emission from the inner part of the torus. In type 2 AGN, the inner hot dust is obscured by cooler dust at larger distances from the AGN. This difference in observed dust temperature should lead to differences in the spectral color (but see Sect. 5.2). On the other hand, since hot dust is expected to show the silicate feature in emission and cold (optically-thick) dust to show a silicate absorption feature, spectral index α and silicate feature strength F_{Si}/F_c are supposed to be correlated. In the middle panel of Fig. 11 we plot $\log F_{\text{Si}}/F_c$ against the mid-IR flux ratio $\log F_{\nu}(12.5\ \mu\text{m})/F_{\nu}(8.5\ \mu\text{m})$ and spectral index α . The type 1 AGN do not show a dependence of the silicate feature strength on the spectral index while a range of $\alpha = -0.8 \dots -2.2$ is covered. Apparently the different spectral indices are not an effect of obscuration (assuming that the silicate feature depth is tracing the line-of-sight obscuration to some degree because the tori are seen face-on). Instead it may be a signpost of different dust distributions. We showed in [Hönig & Kishimoto \(2010\)](#) that the spectral slope in the mid-IR is quite sensitive to the power law index a of the radial dust distribution $\eta_r \propto r^a$, where r is the distance from the AGN. The steeper the distribution (i.e. dust

more concentrated to the inner part of the torus), the bluer the mid-IR SED. On the other hand, if the dust distribution is shallower, the mid-IR is redder. Based on these models, we conclude that the type 1 AGN in our sample show some variety in their radial dust distribution, becoming steeper from right to left in this plot. We will pick-up this suggestion when modeling our data in Sect. 6.

The type 2 AGN show some weak trend of redder colors with deeper silicate absorption features. The only exception is NGC 7582 where the silicate feature is much deeper for the given α than in the rest of the objects. Again, this might be connected to additional absorption outside the torus (see above). The nominal relation between silicate feature strength and spectral steepness for type 2s is $\log F_{\text{Si}}/F_c \propto (-0.85 \pm 0.20) \times \log F_{\nu}(12.5 \mu\text{m})/F_{\nu}(8.5 \mu\text{m})$ (excluding NGC 7582), or expressed as spectral index, $\log F_{\text{Si}}/F_c \propto (0.14 \pm 0.03) \cdot \alpha$ (Spearman rank $\rho = -0.88$, null-hypothesis probability 1.6×10^{-3}). This result agrees at least qualitatively with what we expect from a clumpy dust torus around the AGN. Finally, we can test how well the observed obscuration properties in X-ray and the mid-IR are related. In the right panel of Fig. 11 we plot the observed silicate feature strength F_{Si}/F_c in the mid-IR against the Hydrogen column densities N_{H} observed in the X-rays. Despite some scatter, we find a correlation $F_{\text{Si}}/F_c \propto (0.12 \pm 0.03) \times \log N_{\text{H}}$ (Spearman rank -0.71 , null-hypothesis probability 9.9×10^{-4}), which is shown as a dashed line in Fig. 11. This is consistent with the analysis of Shi et al. (2006) who used *Spitzer* data at lower spatial resolution. The ratio F_{Si}/F_c can be converted into an *observed* optical depth τ_{silicate} in the silicate feature, and we define $F_{\text{Si}}/F_c = \exp(-\tau_{\text{silicate}})$ (see right *y*-axis in Fig. 11 and data in Table 6). In this way the correlation between observed silicate feature depth and Hydrogen column density becomes

$$\tau_{\text{silicate}} = (0.00 \pm 0.73) + (0.14 \pm 0.03) \times \log N_{\text{H},22}, \quad (2)$$

where $N_{\text{H},22}$ is N_{H} in units of 10^{22} cm^{-2} . The observed scatter in this correlation may be a signpost of a clumpy torus where type 1 and type 2 AGN are less differentiated. We recall again that the *observed* τ_{silicate} is not the same as the *actual* optical depth along the line-of-sight but reflects the complicated radiative transfer inside the torus. Indeed, based on clumpy torus models we expect that the *actual* optical depth along the line-of-sight is much stronger correlated with N_{H} unless a sizable fraction of the Hydrogen column is located inside the sublimation radius (e.g. within the broad-line region). Note that NGC 7582 was excluded from this analysis due to the concerns mentioned above.

Based on the discussion in Sect. 4.3, it is possible that the silicate emission features have a different peak wavelength than the center of the silicate absorption features. This could potentially change the outcome of our analysis on the silicate feature strength relations. In order to investigate this possibility, we extracted F_{Si}/F_c at $10.3 \mu\text{m}$ instead of $9.8 \mu\text{m}$ for the type 1 subsample. The resulting feature strengths are plotted as gray circles in the right panel of Fig. 11. Changes to the original analysis are only moderate and the resulting correlation is shown as a gray-dotted line. The results remain consistent within error bars (here, $F_{\text{Si}}/F_c \propto (0.14 \pm 0.03) \times \log N_{\text{H}}$, Spearman rank $\rho = -0.74$, null-hypothesis probability 4.5×10^{-4}). Thus, our general analysis does not suffer significantly from any possible shift of the central wavelength in silicate emission features.

6. Modeling the data with 3D clumpy torus models

6.1. Constraining torus parameters from VISIR N-band spectro-photometry of nearby AGN

In Hönig & Kishimoto (2010) we investigate the interpretation of mid-IR observations of AGN with our 3D clumpy torus model (Hönig et al. 2006). General dependencies of SEDs and interferometric visibilities on different model parameters have been discussed and it has been shown that the mid-IR SEDs are most sensitive to (1) the radial distribution of dust clouds which we parametrize as a power-law $\eta_r(r) \propto r^a$ (for details please see Sect. 2.5 in Hönig & Kishimoto 2010) and (2) the obscuration inside the torus. The torus-internal obscuration is parametrized by the average number of clouds, N_0 , along an *equatorial* line-of-sight. We remind the reader that N_0 is *not* equal to the number of clouds along the *actual* line-of-sight unless the torus is seen edge-on. We argued that SEDs may serve as a tool to constrain a and maybe N_0 if the strength of the silicate feature and the spectral slope in the mid-IR are simultaneously taken into account.

The mid-IR data presented in this paper have quite a small wavelength coverage from approximately 8–13 μm . This limits the possibilities of modeling IR SEDs, e.g. as recently done for NGC 1068 (Hönig et al. 2008b). As mentioned in the previous section, the two main observational parameters that we can derive from our VISIR data are the spectral index α of the mid-IR continuum and the depth of the silicate feature F_{Si}/F_c (or translated into an observed optical depth τ_{silicate}). In the middle panel of Fig. 11 we plotted both parameters against each other and discussed the observed properties of the type 1 and type 2 subsamples. Now we want to compare these observed mid-IR properties to our torus models and see if we can constrain parameters. For that we simulated a model grid varying a and N_0 for inclinations from $i = 0^\circ$ (pole-on) to 90° . As discussed in Hönig & Kishimoto (2010), other model parameters do not have a significant influence on the SED, except for the half-opening angle θ_0 of the torus, which we discuss below. For the moment we use the common assumption of $\theta_0 = 45^\circ$.

In Fig. 12 we show model predictions for the silicate feature strength F_{Si}/F_c (or observed optical depth τ_{silicate} in the silicate feature) and the spectral index α of the mid-IR continuum. In the left panel, we show simulations for an inclination angle of $i = 30^\circ$ which reflects a typical type 1 AGN line-of-sight for a half opening angle of $\theta_0 = 45^\circ$. Model results for different radial power law indices are color-coded from $a = -2.0$ (blue) to $a = 0.0$ (orange). For each a , several values for N_0 have been calculated and are marked by different symbols in the plot from $N_0 = 2.5$ (asterisks) to $N_0 = 10$ (*x*-shapes). Dashed-colored lines connect symbols with the same a but varying N_0 , while dotted-black lines represent the same N_0 for different a values. The right panel of Fig. 12 shows the same model grid but for a typical type 2 inclination of $i = 75^\circ$. We also overlaid the grid for $i = 60^\circ$ to illustrate how inclination effects change the results. In general, changing a has a strong effect on the spectral index α (as discussed in Hönig & Kishimoto 2010) and some effect on F_{Si}/F_c . On the other hand, varying N_0 and i has almost no effect on α but changes F_{Si}/F_c . It is remarkable that the spectral index α is very insensitive to the torus inclination, even when changing from edge-on to face-on line-of-sights. As discussed, this is characteristic for clumpy models. The gray arrows in Fig. 12 are intended to help the reader, summarizing the rough trends of how the different parameters change the place of an object in the model grid.

The model grids in Fig. 12 illustrate that some fundamental parameters of the dust torus can be constrained even with

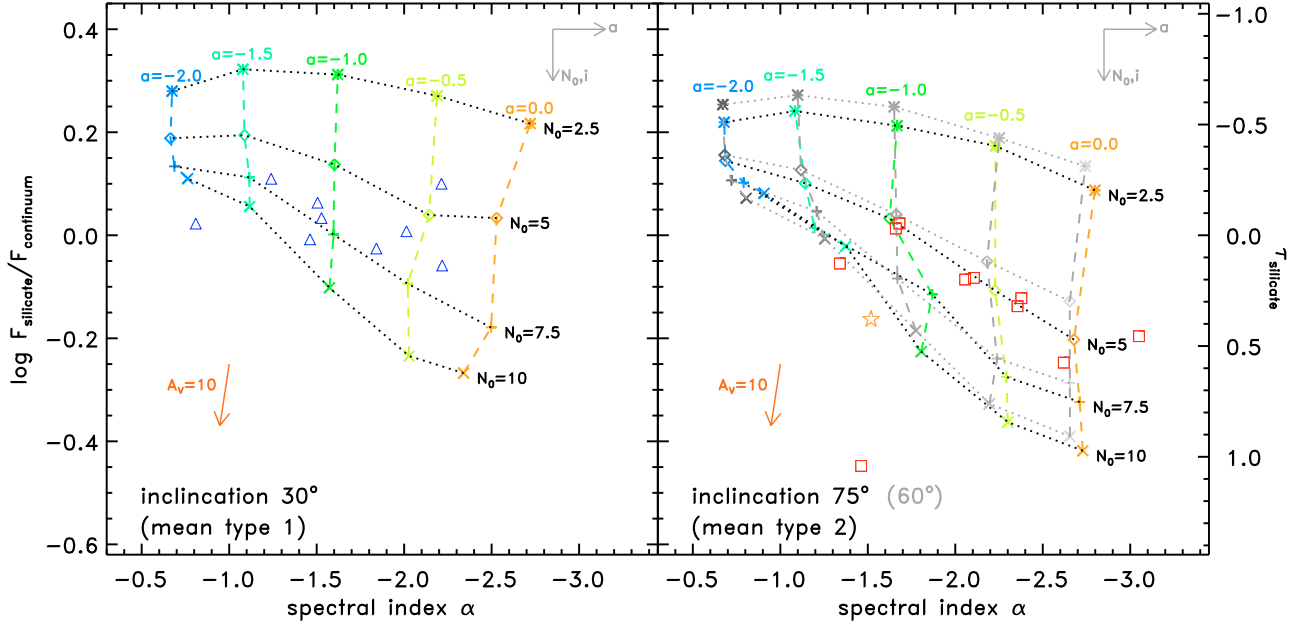


Fig. 12. Comparison of observed mid-IR properties of our type 1 and type 2 AGN to model SEDs simulated with our 3d clumpy torus model. *Left:* F_{Si}/F_c and τ_{silicate} of the type 1 sub-sample (blue triangles) plotted against the spectral index α of the mid-IR continuum emission. Overplotted are model predictions for parameters ranging from $a = 0.0$ (orange) to $a = -2.0$ (light blue) and $N_0 = 2.5$ (asterisks) to $N_0 = 10$ (x-shapes) for a mean type 1 inclination of $i = 30^\circ$. The black arrows note the directions in which the model points change when varying a , N_0 , and i . *Right:* F_{Si}/F_c and τ_{silicate} of the type 2 sub-sample (red squares) plotted against the spectral index α of the mid-IR continuum emission. Overplotted are model predictions for parameters ranging from $a = 0.0$ (orange) to $a = -2.0$ (light blue) and $N_0 = 2.5$ (asterisks) to $N_0 = 10$ (x-shapes) for a mean type 2 inclination of $i = 75^\circ$ (colored symbols) and $i = 60^\circ$ (gray symbols), illustrating the inclination effect). The gray arrows are a rough illustration as a guide for the reader in which direction the model points mostly change when increasing a , N_0 , and i . For reference, NGC 1068 is shown as an orange star, based on the mid-IR spectrum from Mason et al. (2006).

the limited wavelength range covered by our observations. We overplot the type 1 and type 2 sub-samples in the left and right panel of Fig. 12, respectively, to see which region in parameter space is occupied. As already discussed, the most robust constraint can be put on a because it is the almost exclusive parameter to determine an object’s place in the horizontal direction. The type 1 AGN in the left panel populate the range between $a = 0.0$ to $a = -1.5$, with some clumping roughly at -1.0 ± 0.5 . The source ESO 323–G77 is the only exception being located between $a = -1.5$ and $a = -2.0$ but outside the displayed model grid. It is discussed in more detail below. Interestingly, most type 1s also cover a rather narrow range in vertical direction, somewhere between $N_0 = 5$ and 7.5 , and they follow approximately a line of equal N_0 for varying a . The object NGC 7213 is slightly above the other objects, suggesting a lower value for N_0 . Because it is not a classical Seyfert galaxy but a LINER, the offset from the Seyfert 1s could indicate some intrinsic difference in the dust structure. On the other hand, it may also result from an inclination effect: if NGC 7213 is seen more pole-on than the other objects, we would expect that for the same a and N_0 the object is placed slightly above the others (see also inclination effect illustrated in the right panel of Fig. 12). However, at low inclinations any viewing-angle effect is small and not able to explain all of the offset of NGC 7213.

The right panel of Fig. 12 shows the type 2 AGN of our sample. Most objects are again located between $a = 0.0$ and $a = -1.5$ and follow the line of constant $N_0 = 5$ for inclination $i = 75^\circ$ or $N_0 \sim 6$ for $i = 60^\circ$. There are however a number of outliers from this plot, most notably NGC 7582. For this galaxy we already remarked that additional extinction from a circumnuclear star-burst ring might interfere with the emission from the nucleus. Consequently, the observed mid-IR properties

are not generic properties of the torus emission. To study the possibility if such additional (screen) absorber may be responsible for outlier in the plot, we used the extinction curves of our dust composition (ISM dust with Ossenkopf silicates; see Hönl & Kishimoto 2010, for details) and derived the change of mid-IR spectral properties for $A_V = 10$. The resulting shift is shown as an orange arrow in both panels of Fig. 12. Actually NGC 7582 and MCG–5–23–16 – the objects in our sample which are located below the model grid – have a comparably high inclination of the host-galaxy, which may contribute some extinction screen to the nuclear emission. On the other hand, MCG–5–23–16 is very close to the model grid and the offset can be easily explained by either a torus inclination $i > 75^\circ$ or a torus with $N_0 = 10$ or slightly higher. Please note that “reddening” (extinction) actually makes the N -band mid-IR colors slightly bluer, which is an effect of the extinction curve at these wavelengths. Another interesting object is NGC 5643. This low-luminosity AGN has the reddest colors in our sample. It follows quite well the line of constant N_0 occupied by the other AGN, but is placed at $a > 0.0$. This would imply that the torus is much more extended than in the other objects compared to the intrinsic scale, something that might be tested by IR interferometry.

Finally we will discuss ESO 323–G77, which is an outlier in the type 1 plot (left panel of Fig. 12). It is located slightly below the model grid between $a = -1.5$ and -2.0 . Based on our modeling, the offset cannot be explained by either an inclination effect or a higher N_0 . Inclination is excluded since ESO 323–G77 is even below the type 2 AGN model grid in the left panel of Fig. 12. Moreover, for such steep dust distributions, most clouds are located in the innermost part of the torus close to the sublimation radius. Adding more clouds to the torus will dramatically increase the torus-internal obscuration and moves the models

rather to the right than downward in the plot. This effect can already be seen in the model grid for $a = -2.0$ and $N_0 = 10$ and becomes even stronger for higher N_0 . On the other hand, ESO 323–G77 is showing some absorption pattern in the optical and the X-rays (see Table 1), which could result in a down-left drift in the plot (see orange arrow). It is located in the same area of the $L_{\text{MIR}} - L_X$ -correlation as MCG–3–34–64 and IC 5063, for which we found extended emission probably coming from the NLR. Because ESO 323–G77 is a type 1 AGN with a more or less face-on line-of-sight, dust in the NLR can cause screen extinction, which may explain the offset position in Fig. 12. In this case it is reasonable to conclude from Fig. 12 that the intrinsic dust distribution power-law index of ESO 323–G77 is most likely somewhere between $a = -1.5$ and -2.0 as expected from the relatively blue mid-IR color.

In summary, based on our modeling we find that the Seyfert galaxies in our sample have a torus with a rather shallow radial dust distribution with a typical power law index of approximately $a = -1 \pm 0.5$. This parameter is quite solidly constrained by the mid-IR spectral indices. For the presented model grid we also found a typical range for the average number of clouds along an equatorial line-of-sight of $N_0 \sim 5\text{--}8$ for the whole sample. It is however difficult to pin down this parameter for each individual object because inclination effects can slightly alter the results. As yet we have not discussed how the vertical structure of the torus (represented by the half-opening angle, θ_0 , of the torus) influences the models. Actually θ_0 does not have an effect on the horizontal position of the object (exclusively determined by a) but can change its vertical position, i.e. the strength of the silicate feature. We found that increasing θ_0 from 45° to 60° has a similar effect as decreasing the inclination angle by about 15° . If we consider $\theta_0 = 45^\circ$ as a reasonable *sample average*, the range of $N_0 \sim 5\text{--}8$ found as a typical value for the whole sample is still valid, although it might be complicated to constrain N_0 , θ_0 , and i for each *individual* object.

6.2. Comparison to IR interferometry

While our modeling approach based on the spectral slope and silicate feature strength is very limited in wavelength range, we can test its results and predictions. For that we compared the derived radial dust distribution to recent results from IR interferometry. In Kishimoto et al. (2009a), we argued that IR interferometry of type 1 AGN can be used to determine the surface brightness profile of the dust torus. For that the N -band visibilities observed by VLTI/MIDI were plotted against an object-intrinsic spatial scale (the near-IR reverberation radius, which is presumably indicative for the inner boundary of the dust distribution). It was found that the brightness profile in NGC 3783 depends on the radius $\propto r^{-2}$. We can now try to reproduce this finding by our models with the model parameters as constrained by Fig. 12. For NGC 3783 we find that $a \sim -0.75$ and $N_0 \sim 7$ for $i = 30$. Based on these parameters, we simulated images and calculated corresponding mid-IR visibilities. The results at $8.5 \mu\text{m}$ and $12.5 \mu\text{m}$ are shown in Fig. 13. The model visibilities generally agree with the available data, despite some overestimation of the visibility at longer wavelengths for the long projected baseline (baseline length 65 m, PA 120°). That the observed visibilities are lower in PA 120° may be due to some elongation of the source. Based on our clumpy torus models we would not expect that the torus itself produces these kind of deviation. Interestingly the larger size in PA 120° is pointing in a similar direction as the polarization angle ($\theta_{\text{pol}} \sim 135^\circ$ Smith et al. 2002), which implies that the mid-IR nucleus is elongated *towards the NLR*. This may

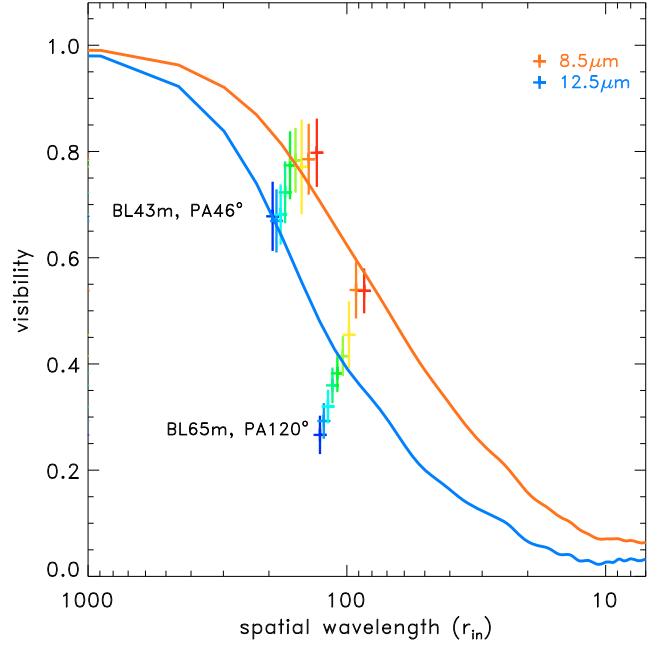


Fig. 13. Comparison of the VLTI/MIDI 8–13 μm interferometry of NGC 3783 with our 3D clumpy torus models. The interferometry data at projected baseline length 65 m were reported by Beckert et al. (2008), the 43 m data were presented in Kishimoto et al. (2009a). We plot the observed 8–13 μm visibility (color-coded from red to blue) against the spatial wavelength in units of the inner radius r_{in} (see Kishimoto et al. 2009a, for details). Overplotted are the model visibilities for $8.5 \mu\text{m}$ (red line) and $12.5 \mu\text{m}$ (blue line) based on model parameters derived from Fig. 12 ($a = -0.75$, $N_0 = 7$). The $8.5 \mu\text{m}$ and $12.5 \mu\text{m}$ data have the same colors as the corresponding model.

place NGC 3783 into the same group of objects as IC 5063 and MCG–3–34–64, which show some contribution from the NLR to the mid-IR emission (although for NGC 3783 on much smaller scale and fraction), in particular to longer wavelengths. We leave a more detailed analysis of the interferometric measurements to a more extended dataset that was recently obtained (Hönig et al., in preparation). Despite these details, NGC 3783 as a case study illustrates that the brightness profiles of the dust distribution are strongly connected with the mid-IR slope α , and both are very sensitive to the radial distribution of the dust.

In the left panel of Fig. 12, we also show NGC 1068 as an orange asterisk. It is located slightly below the $i = 75^\circ$ model grid in the range of $a = -1.0 \dots -1.5$ and $N_0 \sim 10$. Recently we presented detailed modeling of the full IR SED of NGC 1068 at high-spatial resolution simultaneously with near- and mid-IR interferometry (Hönig et al. 2006, 2007, 2008b). Since IR interferometry resolves the spatial brightness profile, it is considered as very constraining for model parameters. For NGC 1068 we found typical parameters of $a \sim -1.5$, $i = 70\text{--}90^\circ$, and $N_0 \sim 10$ which excellently agrees with the analysis presented here based on the mid-IR spectral index and the silicate feature strength.

In summary we find that the results from our analysis of the mid-IR spectral index α and the silicate feature strength agrees well with results from IR interferometry. Model parameters derived by our spectro-photometry approach are consistent with a much more detailed analysis of the IR emission of NGC 1068 and can reproduce interferometric measurements of NGC 3783. In turn, based on the analysis of the mid-IR spectra, we can make predictions about the spatial brightness profiles of AGN for interferometry. For instance, we expect that ESO 323–G77

and MARK 509 have quite compact profiles (i.e. high visibility) while objects like NGC 3227, NGC 7213, or NGC 7469 have rather extended profiles (i.e. low visibilities) when scaled for their intrinsic radii.

6.3. A luminosity dependence of the torus properties?

One interesting aspect of the torus is whether or not there are any differences in its structure at low and high AGN luminosity. Obscuration statistics of type 1 and type 2 AGN suggest that the relative fraction of type 1 AGN increases with luminosity (e.g. Simpson 2005; Maiolino et al. 2007; Hasinger 2008). This phenomenon is commonly explained by a decrease of the torus covering factor with luminosity – and referred to as the “receding torus”. On the other hand, if the covering factor decreases, the “reprocessing ratio” $L_{12\ \mu\text{m}}/L_X$ ratio is also expected to decrease because less torus surface is heated by the AGN. However, based on the $L_{\text{MIR}} - L_X$ -correlation by Gandhi et al. (2009), we find that $L_{12\ \mu\text{m}}/L_X \propto L_X^{0.11 \pm 0.07}$, which means that the reprocessing ratio does not significantly change with luminosity (maybe marginally increases; but we note that when using the bolometric luminosity instead of L_X , the ratio might slightly decrease with luminosity, depending on the bolometric correction used; see also Gandhi et al. 2009, Sect. 4.5). In Hönic & Beckert (2007) we suggested a possibility to explain these observations: increasing AGN radiation pressure may cause large dust clouds to be driven out of the torus at higher luminosities. Consequently, the absorbing column towards the AGN decreases and it becomes less likely that the line-of-sight towards the nucleus is obscured. On the other hand, the covering factor and reprocessing ratio will not change.

The question remains though whether there are direct hints that the torus dust distribution changes with luminosity. The most direct way of probing this possibility is, of course, IR interferometry. On the other hand, due to the sensitivity of current interferometers, one is limited to few objects and the luminosity coverage is limited. In the previous sections we showed that the radial structure of the torus and the torus-internal obscuration properties can be constrained by simultaneously comparing the mid-IR spectral index α and the silicate feature strength. In particular, constraining the radial power-law index a using α seems to be quite solid (see also Sect. 6.2).

The AGN in our sample have typical luminosities of nearby Seyfert galaxies, i.e. in the range of 10^{42} erg/s to 10^{45} erg/s, and conclusions drawn about the typical torus properties of $a = -1 \pm 0.5$ and $N_0 = 5-8$ are only valid for these luminosities. Recently, Polletta et al. (2008) presented rest-frame near-to-mid-IR SEDs of 23 type 2 QSOs with luminosities between 10^{46} erg/s to several 10^{47} erg/s. Interestingly, most of them showed quite blue IR spectral indices. Using the clumpy torus models, it was concluded that the typical radial power-law indices in the type 2 QSOs were tracing a quite steep dust distribution, with $a \sim -2 \dots -3$. If this is indeed a typical value for luminous AGN, it is much steeper than what we find in our intermediate-luminosity sample. Consequently there could be a change of the torus structure with luminosity.

At the low-luminosity end, we do not have a good coverage of mid-IR data where spatial resolution is sufficient to isolate the torus emission. But we can compare the lower-luminosity objects in our sample to those at the higher luminosity end. Indeed, in Sect. 5.2 we note that the reddest objects in both type 1 and type 2 sub-samples are those with the lowest luminosities (NGC 3227 and NGC 7213 for type 1s, NGC 5643 and ESO 428-G14 for the type 2s). This would suggest that

the lower-luminosity AGN have much more shallow dust distributions, i.e. the torus is relatively more extended compared to higher-luminosity objects. If true, we might see an imprint of this behavior in the mid-IR size-luminosity relation, e.g. as it can be constructed from interferometry. The prediction would be that for a sufficiently large sample the relation does not scale as $r \propto L^{1/2}$ but with a slightly smaller power-law index. Similarly, near-IR interferometric sizes would be systematically larger than IR reverberation-mapping radii at lower luminosities, and would better match each other at higher luminosities (cf. Kishimoto et al. 2009b, for Keck interferometry results of four objects).

7. Summary

We presented high-spatial resolution mid-IR spectro-photometry of a sample of nearby AGN. Based on the selection criteria, the sample cannot be considered complete but the objects are typical for local intermediate-luminous AGN, i.e. Seyfert 1 and Seyfert 2 galaxies ranging from Compton-thin to Compton-thick X-ray obscuration. The ground-based mid-IR data were taken with the VLT mid-IR imager and spectrograph VISIR and it represents to our knowledge the largest sample of mid-IR N -band spectra of AGN with angular resolution $\leq 0''.4$. The main characteristics of these data are:

- Our ground-based observations isolate the nuclear dust emission of the torus from host-galactic sources. PAH emission features, commonly associated with star-formation in the host galaxy, are mostly absent in our data (i.e. at spatial scales < 100 pc), although seen in *Spitzer* data at lower spatial resolution. We showed that subtracting the nuclear VISIR emission from the *Spitzer* data reveals spectra reminiscent of a star-formation template.
- The mid-IR spectra show only moderate silicate features. While silicate absorption is easily identified in type 2 AGN, the corresponding emission feature in type 1 AGN is very weak, if present at all. Thus, the weakness of the silicate feature is an intrinsic property of the emitting region, which is $< 25-160$ pc, depending on the object. This points to an origin in the circumnuclear dust distribution – the “dust torus”.
- The strongest silicate emission features are seen in the type 2 AGN NGC 2110 (see also Mason et al. 2009) and the broad-line LINER NGC 7213. We analyzed the silicate emission feature of the latter object and found a shift of central wavelength of the silicate feature to $\sim 10.5\ \mu\text{m}$. This shift is probably not exclusively caused by radiative transfer effects due to absorption as recently suggested, but could indicate different dust composition than in the standard ISM, or a radial change of grain size and/or chemistry in the dust distribution.

The observed mid-IR luminosities were compared to other AGN luminosity tracers, namely the 2–10 keV luminosity L_X and the luminosity of the [O III]($\lambda 5007\ \text{\AA}$) narrow emission line. We showed that correlations of both tracers with $L_{12\ \mu\text{m}}$ are quite strong and tighter than between L_X and $L_{[\text{O III}]}$. It may be worthwhile considering $L_{12\ \mu\text{m}}$ as an isotropic AGN luminosity tracer.

Three objects in our sample, MCG-3-34-64, ESO 323-G77, and IC 5063, are outliers in the otherwise tight $L_{\text{MIR}} - L_X$ -correlation (Horst et al. 2008; Gandhi et al. 2009). We evaluated mid-IR images in four different filters per object and found that they show significant extension and elongation. In IC 5063, the elongation direction is consistent with HST [O III] emission maps. We suggest that a sizable fraction of the mid-IR emission in these objects is originating in the

narrow-line region, possibly caused by dust located there, similar to the mid-IR-bright NLR in NGC 1068. This additional emission may be the reason for the mid-IR “overluminosity” in the $L_{\text{MIR}} - L_X$ -correlation.

Because the wavelength range covered by our data is limited to 8–13 μm , the main properties we can use for analyzing the dust emission are (1) the mid-IR continuum spectral index α ; and (2) the strength of the silicate feature. We found that there are at best mild trends of increasing α with increasing $L_{12\ \mu\text{m}}$ and increasing α with increasing Hydrogen column density N_{H} . The weak trend of the α vs. N_{H} shows that strong or weak obscuration does not have a significant impact on the overall color of the mid-IR SED, consistent with the as yet not detected difference between the $L_{\text{MIR}} - L_X$ -correlation of type 1 and type 2 AGN (see also Gandhi et al. 2009). As suggested in Hönig & Kishimoto (2010), the distribution of the dust around the AGN has much more impact on the mid-IR spectral slope than obscuration or orientation effects. We also compared the strength of the silicate feature F_{Si}/F_c (or observed τ_{silicate}) to the mid-IR luminosity and the Hydrogen column density. We find a similar correlation of silicate feature strength and N_{H} as Shi et al. (2006), corresponding to $\tau_{\text{silicate}} \propto 0.14 \times \log N_{\text{H}}$. Interestingly, there might be a difference between silicate feature strength at lower and higher luminosity in our sample: type 1 and type 2 objects at lower $L_{12\ \mu\text{m}}$ seem to show a stronger difference in silicate features than objects at higher $L_{12\ \mu\text{m}}$, where type 1 and type 2 features appear rather similar. A larger sample of objects with high angular resolution is required to see if the trend can be confirmed.

Next, we plotted the silicate feature strength against mid-IR spectral index α . This analysis was motivated by our 3D clumpy torus model where we found that simultaneously accounting for silicate feature and spectral slope may be very constraining for torus parameters. We overplotted the observed properties of type 1 and type 2 AGN with predictions from our model, varying (1) the radial dust distribution power law index a (radial distribution $\eta_r \propto r^a$); (2) the average number of clouds N_0 along the line-of-sight in the equatorial plane; and (3) the torus inclination i . Our main conclusions are:

- α versus silicate-feature-strength plots are quite constraining for torus parameters because α is almost exclusively sensitive to a and the silicate strength is mostly sensitive to N_0 and i . We discussed how the position of an object is depending on these and possible other model parameters and concluded that a can be constrained for each individual object, while N_0 may be better derived as a sample mean.
- For our Seyfert sample, we find typical values of $a = -1.0 \pm 0.5$ and $N_0 = 5-8$. The sample average values are similar for type 1 and type 2 AGN, which is a support for the unification scheme. We note, however, that this conclusion is only valid for typical Seyfert AGN as presented in our study.
- Some objects may be suffering from extinction in the host galaxy. In such cases, however, additional screen absorption changes mostly the object’s vertical position in the α -silicate strength plot.
- The approach of constraining a and N_0 based on the mid-IR spectral index α and the silicate features strength was tested for examples where we also have much broader IR SEDs and/or infrared interferometry (NGC 1068 and NGC 3783). Interferometry directly traces the brightness distribution of the emission region and is most sensitive to the radial distribution of the dust (see Kishimoto et al. 2009a). We find that the model parameters derived from simultaneous SED and

interferometry modeling of NGC 1068 are consistent with parameters derived from the α -silicate feature plot. In addition, α and silicate-feature-strength parameters derived for NGC 3783 are able to reproduce the available mid-IR interferometric data. Based on our mid-IR single-telescope data, it is possible to make predictions for interferometry.

Finally, we discussed a possible change of torus properties with luminosity. Based on a comparison with literature data and modeling, we found evidence that the dust tori might be more compact (i.e. $a \approx -2 \dots -3$) for high luminosity AGN and shallower on the low-luminosity end ($a \approx 0.0 \dots -0.5$), but we need better selected samples to confirm this trend. If true, this change of the dust distribution in the torus will slightly alter the mid-IR size-luminosity relation and cause differences when comparing near-IR interferometric sizes with near-IR reverberation mapping radii of AGN.

Acknowledgements. We thank the anonymous referee for valuable suggestions which led to significant improvements. The paper was in part supported by Deutsche Forschungsgemeinschaft (DFG) in the framework of a research fellowship (“Auslandsstipendium”) for SH. P.G. is supported by JSPS and RIKEN Foreign postdoctoral fellowships. This research made use of the NASA/IPAC Extragalactic Database (NED) operated by the JPL (Caltech), under contract with NASA.

References

- Antonucci, R. 1993, ARA&A, 31, 473
 Beckert, T., Driebe, T., Hönig, S. F., & Weigelt, G. 2008, A&A, 486, L17
 Beckmann, V., Gehrels, N., Shrader, C. R., & Soldi, S. 2006, ApJ, 638, 642
 Bennert, N., Jungwiert, B., Komossa, S., Haas, M., & Chini, R. 2006, A&A, 459, 55
 Bentz, M. C., Peterson, B. M., Netzer, H., Pogge, R. W., & Vestergaard, M. 2009, ApJ, 697, 160
 Bianchi, S., Guainazzi, M., Mattm, G., et al. 2005, A&A, 442, 185
 Burtscher, L., Jaffe, W., Raban, D., et al. 2009, A&A, 705, L53
 Chiar, J. R., & Tielens, A. G. G. M. 2006, ApJ, 637, 774
 Dadina, M. 2007, A&A, 461, 1209
 Della Ceca, R., Severgnini, P., Caccianiga, A., et al. 2008, MmSAI, 79, 65
 de Grijp, M. H. K., Keel, W. C., Miley, G., Goudfroofij, P., & Lub, J. 1992, A&AS, 96, 389
 Denney, K. D., Bentz, M. C., Peterson, B. M., et al. 2006, ApJ, 653, 152
 Draine, B. T., & Lee, H. M. 1984, ApJ, 285, 89
 Dullemond, C. P., & van Bemmell, I. M. 2005, A&A, 436, 47
 Efstathiou, A., & Rowan-Robinson, M. 1995, MNRAS, 273, 649
 Elvis, M., Wilkes, B. J., McDowell, J. C., et al. 1994, ApJS, 95, 1
 Gandhi, P., Horst, H., Smette, A., et al. 2009, A&A, 502, 457
 Glass, I. S. 1992, MNRAS, 256, 23
 Glass, I. S. 2004, MNRAS, 350, 1049
 Granato, G. L., & Danese, L. 1994, MNRAS, 268, 235
 Gu, Q., Melnick, J., Fernandes, R., et al. 2006, MNRAS, 366, 480
 Haas, M., Siebenmorgen, R., Pantin, E., et al. 2007, A&A, 473, 369
 Hao, L., Spoon, H. W. W., Sloan, G. C., et al. 2005, ApJ, 625, L75
 Hao, L., Weedman, D. W., Spoon, H. W. W., et al. 2007, ApJ, 655, L77
 Hasinger, G. 2008, A&A, 490, 905
 Hönig, S. F., & Beckert, T. 2007, MNRAS, 380, 1172
 Hönig, S. F., & Kishimoto, M. 2010, A&A, submitted [arXiv:0909.4539]
 Hönig, S. F., Beckert, T., Ohnaka, K., & Weigelt, G. 2006, A&A, 452, 459
 Hönig, S. F., Beckert, T., Ohnaka, K., & Weigelt, G. 2007, ASPC, 373, 487
 Hönig, S. F., Smette, A., Beckert, T., et al. 2008a, A&A, 485, L21
 Hönig, S. F., Prieto, M. A., & Beckert, T. 2008b, A&A, 485, 33
 Horst, H., Smette, A., Gandhi, P., & Duschl, W. J. 2006, A&A, 459, L17
 Horst, H., Gandhi, P., Smette, A., & Duschl, W. J. 2008, A&A, 479, 389
 Horst, H., Duschl, W. J., Gandhi, P., & Smette, A. 2009, A&A, 495, 137
 Jaffe, W., Meisenheimer, K., Röttgering, H. J. A., et al. 2004, Nature, 429, 47
 Kishimoto, M., Hönig, S. F., Beckert, T., & Weigelt, G. 2007, A&A, 476, 713
 Kishimoto, M., Hönig, S. F., Tristram, K., & Weigelt, G. 2009a, A&A, 493, L57
 Kishimoto, M., Hönig, S. F., Antonucci, R., et al. 2009b, A&A, 507, L57
 Krabbe, A., Böker, T., & Maiolino, R. 2001, ApJ, 557, 626
 Krügel, E. 2008, An introduction to the physics of interstellar dust, Boca Raton
 Levenson, N., Sirocky, M. M., Hao, L., et al. 2007, ApJ, 654, L45
 Levenson, N., Radomski, J. T., Packham, C., et al. 2009, ApJ, 703, 390

- Lutz, D., Maiolino, R., Spoon, H. W. W., & Moorwood, A. 2004, *A&A*, 418, 465
- Maiolino, R., Salvati, M., Bassani, L., et al. 1998, *A&A*, 338, 781
- Maiolino, R., Shemmer, O., Imanishi, M., et al. 2007, *A&A*, 468, 979
- Malizia, A., Landi, R., Bassani, L., et al. 2007, *ApJ*, 668, 81
- Martinez-Sansigre, A., Karim, A., Schinnerer, E., et al. 2009, *ApJ*, 706, 184
- Mason, R. E., Geballe, T. R., Packham, C., et al. 2006, *ApJ*, 640, 612
- Mason, R. E., Levenson, N. A., Shi, Y., et al. 2009, *ApJ*, 693, L136
- Meléndez, M., Kraemer, S. B., Armentrout, B. K., et al. 2008, *ApJ*, 682, 94
- Nelson, C. H., Green, R. F., Bower, G., & Gebhardt, K. 2004, *ApJ*, 615, 652
- Nenkova, M., Ivezić, Ž., & Elitzur, M. 2002, *ApJ*, 570, L9
- Nenkova, M., Sirocky, M. M., Nikutta, R., Ivezić, Z., & Elitzur, M. 2008, *ApJ*, 685, 160
- Netzer, H., Mainieri, V., Rosati, P., & Trakhtenbrot, B. 2006, *A&A*, 453, 525
- Nikutta, R., Elitzur, M., & Lacy, M. 2009, *ApJ*, 707, 1550
- Ossenkopf, V., Henning, T., & Mathis, J. S. 1992, *A&A*, 261, 567
- Pier, E. A., & Krolik, J. H. 1993, *ApJ*, 418, 673
- Polletta, M., Weedman, D. W., Hönig S. F., et al. 2008, *ApJ*, 675, 960
- Raban, D., Jaffe, W., Röttgering, H., Meisenheimer, K., & Tristram, K. R. W. 2009, *MNRAS*, 394, 1325
- Roche, P. F., Packham, C., Aitken, D., & Mason, R. E. 2007, *MNRAS*, 375, 99
- Schartmann, M., Meisenheimer, K., Camenzind, M., et al. 2008, *A&A*, 482, 67
- Schmid, H., Appenzeller, I., & Burch, U. 2003, *A&A*, 404, 505
- Schmitt, H. R., Ulvestad, J. S., Antonucci, R. R. J., & Kinney, A. L. 2001, *ApJS*, 132, 199
- Schmitt, H. R., Donley, J. L., Antonucci, R. R. J., Hutchings, J. B., & Kinney, A. L. 2003, *ApJ*, 148, 327
- Schweitzer, M., Groves, B., Netzer, H., et al. 2008, *ApJ*, 679, 101
- Shi, Y., Rieke, G. H., Hines, D. C., et al. 2006, *ApJ*, 653, 127
- Siebenmorgen, R., Haas, M., Krügel, E., & Schulz, B. 2005, *A&A*, 436, L5
- Simpson, C. 2005, *MNRAS*, 360, 565
- Sirocky, M. M., Levenson, N. A., Elitzur, M., Spoon, H. W. W., & Armus, L. 2008, *ApJ*, 678, 729
- Smith, J. E., Young, S., Robinson, A., et al. 2002, *MNRAS*, 335, 773
- Sturm, E., Schweitzer, M., Lutz, D., et al. 2005, *ApJ*, 629, L21
- Suganuma, M., Yoshii, Y., Kobayashi, Y., et al. 2006, *ApJ*, 639, 46
- Swain, M., Vasisht, G., Akeson, R., et al. 2003, *ApJ*, 596, L163
- Tueller, J., Mushotzky, R. F., Barthelmy, S., et al. 2008, *ApJ*, 681, 113
- Tran, H. D. 2003, *ApJ*, 583, 632
- Tristram, K. R. W., Meisenheimer, K., Jaffe, W., et al. 2007, *A&A*, 474, 837
- Tristram, K. R. W., Raban, D., Meisenheimer, K., et al. 2009, *A&A*, 502, 67
- Urry, C. M., & Padovani, P. 1995, *PASP*, 107, 803
- Veron-Cetty, M. P., & Veron, P. 2006, *A&A*, 455, 773
- Weigelt, G., Wittkowski, M., Balega, Y. Y., et al. 2004, *A&A*, 425, 77
- Winkler, H. 1992, *MNRAS*, 257, 677
- Winkler, H., Glass, I. S., van Wyk, F., et al. 1992, *MNRAS*, 257, 659
- Wold, M., & Galliano, E. 2006, *MNRAS*, 369, L47